Published in POLYMER

Polymer 53 (2012) 1747–1759

Study of change in dispersion and orientation of clay platelets in a polymer nanocomposite during tensile test by variostage small-angle X-ray scattering

Jayita Bandyopadhyay[1], Thomas Malwela[1], and Suprakas Sinha Ray[1,2] *

[1]*DST/CSIR NIC, National Centre for Nano-Structured Materials, Council for Scientific and Industrial Research, Pretoria 0001, Republic of South Africa*

[2]*Department of Chemical Technology, University of Johannesburg, Doornfontein 2018, Johannesburg, Republic of South Africa*

Abstract

To understand the change in dispersion and orientation of clay platelets in three dimensional space during tensile test, neat polymer and its nanocomposite samples were studied by small- and wide-angle X-ray scattering (SWAXS). The samples after tensile tests were examined by tilting and rotating them with respect to the incident X-ray beam and also by scanning them at different positions. The tilt angle measurements provide better understanding on the dispersion and orientation of the clay platelets in nanocomposite. On the other hand, rotation and scanning measurements reveal details information on the orientation of polymer crystal planes due to the tensile stretching and percent crystallinity. Finally, the focussed ion beam electron tomography was employed to support the dispersion and orientation models of clay platelets proposed on the basis of SWAXS analyses.

Keywords: Nanocomposites; Dispersion and orientation; Variostage small- and wide-angle Scattering

* Corresponding author. Fax: +27 12 841 2229; E-mail: rsuprakas@csir.co.za

1. Introduction

The properties of clay-containing polymer nanocomposites are directly related to the properties of the matrix polymer, the properties of the nano-filler, the strength and nature of the interfacial interactions between the polymer matrix and the filler, and finally, the surface area of the interfacial bonds. In the case of nano-filled composite materials, the area of interfacial bond is determined by the aspect ratio of the dispersed particles as well as loading level. As the nanoparticles are more evenly dispersed in the polymer matrix, the thickness of the dispersed particles decreases, and as a result the aspect ratio and the effect of the filler on the matrix mechanical properties increase. One such nanoparticle, extensively used, is montmorillonite (MMT). In pristine form MMT usually contains Na^+ ions and in this form it is only miscible with water soluble polymers. To render MMT miscible with commodity and engineering polymers, MMT is generally ion exchanged with alkyl ammonium or phosphonium cations to obtain organically modified MMT (OMMT). Alkyl ammonium or phosphonium cations lower the surface energy of silicate hosts and improve the compatibility with polymer matrices [1, 2].

Over the last few years, nearly all types of polymer matrices have been used for the preparation of nanocomposites with both pristine and organically modified clays [1–6], and research efforts have produced many interesting results, including some commercial success [7]. In this work, we have used poly[(butylene succinate)-co-adipate] (PBSA) as a model polymer matrix for the preparation of nanocomposite with OMMT. PBSA is a synthetic aliphatic polyester and is synthesized by the polycondensation of butane-1,4-diol in the presence of succinic and adipic acids with relatively low production cost and satisfactory mechanical properties equivalent to that of polyolefins such as polyethylene [8, 9]. The PBSA, compared with poly(butylene succinate) (PBS), is more susceptible to biodegradation because of its lower crystallinity and more flexible polymer chains. It has excellent processibility, so that it can be processed in the field of textiles into melt blow, multifilament, monofilament, flat, and split yarn, and also in the field of plastics into injection-moulded products. It is, thus, a promising polymer for various applications [10].

In recent publications, we have shown that the tensile properties of PBSA increased upon nanocomposite formation with methyl tallow bis(2-hydroxylethyl) quaternary ammonium modified MMT (commercially known as Cloisite®30B, C30B) [11, 12]. During that time we proposed that the high level interactions between the ‘CO’ groups on the PBSA backbone with the diols present in the C30B seem to be responsible for the concurrent improvement of the nanocomposites tensile properties. In a subsequent work, we used small-angle X-ray scattering (SAXS) and local high-resolution transmission electron microscopy (HRTEM) to understand the exact mechanism of enhanced tenacity in a PBSA nanocomposite containing 3 wt% C30B (PBSANC3) [13]. The reason behind this selection was that recent structural characterizations by SAXS and TEM analyses showed that in the case of PBSANC3, silicate layers have enough

available space to orient themselves in PBSA matrix [14]. Results showed that the enhanced tenacity in the case of nanocomposite is due to the orientation of the dispersed clay layers in the direction of the applied tensile strain [13]. Further, this orientation affects the dispersion characteristics in such a way that the intercalated silicate layers overlap. This allows a better energy-dissipation mechanism, which in turn is responsible for the concurrent improvement in tensile properties [13].

Now to fully understand the observed tensile properties of PBSACN3 and also to establish the structure-property relationship of this nanocomposite material, it is very important to visualise their three-dimensional (3D) structure and, in particular, the dispersion/distribution of the clay platelets within the PBSA matrix and the nature of the interfacial interaction between the PBSA and the C30B surface. In order to achieve this goal, we studied the neat PBSA and PBSANC3 samples after tensile test using small- and wide-angle X-ray scattering (SWAXS). The samples were examined in SWAXS by tilting and rotating them with respect to the incident X-ray beam and also by scanning them at different positions. Therefore, this article deals with the following challenges in detail: the dispersion and orientation of clay platelets in PBSA matrix after tensile test, the ordered structure of polymer chains, and finally, polymer crystallinity. To support the SWAXS results, focused-ion-beam electron tomography was employed.

2. Experimental procedure

2.1. Materials and preparation of nanocomposite

The PBSA used in this study is a commercial product from Showa Denko (Japan), with the designation BIONOLLE #3001. Details regarding PBSA physical properties can be found elsewhere [14]. The organoclay used in this study was Cloisite®30B (C30B), purchased from Southern Clay Products. The PBSA nanocomposite (PBSANC) containing 3 wt% of C30B was prepared in a Polylab Thermohaake-batch mixer at 135 ºC (set temperature) and a rotor speed of 60 rpm for 8 min. The dried neat PBSA and nanocomposite strands were injection-moulded using an injection moulding machine (bench-top Haake Minijet II) operated at 135 °C with a mould temperature of 60 °C (ASTM D-638). Neat PBSA and PBSANC samples were annealed at 50 °C under vacuum prior to all characterizations and property measurements.

2.2. Characterization techniques

The tensile modulus, tensile strength, and elongation at break were measured in a tensile Instron 88215 tester (load 5 kN) with the cross head speed of 5 cm/min [13]. The samples after tensile test were analysed by SWAXS. SWAXS experiments were carried out by an Anton Paar SAXSess instrument, operated at 40 kV and 50 mA with a point collimation geometry. The radiation used was a CuK_{α} radiation of wavelength 0.154 nm (PAN analytical X-ray source).

Intensity profiles were obtained with a point collimated SAXSess and recorded with a two-dimensional imaging plate. In order to understand the effect of elongation (during tensile testing) on the dispersion and orientation of clay platelets in the polymer matrix, PBSA and PBSANC samples after tensile tests (refer Fig. 1(a)) were examined with three different experimental set-ups. The vario-stage sample holder allows to tilting (tilt angle measurement), rotating, and scanning samples at different positions with respect to the incident X-ray beam. The sample-to-detector distance for tilt angle measurement, rotation, and scanning were 260.24, 250.24, and 251.24 mm, respectively. The radius of detector curvature was 260 mm. The read-out angles were calculated from the pixel size, and the obtained q scale was cross-checked by measuring silver behenate whose equidistant peak positions are known. SAXS data were collected at room temperature. All samples were exposed under X-ray for 1h in order to check the dispersion characteristic of the silicate particles in the PBSA matrix. The thickness of the samples varied roughly between 0.6 to 0.9 mm.

The experimental set-up for tilt angle measurement (x-axis rotation stage), z-axis rotation, and scanning are presented in Schemes 1, 2, and 3, respectively. According to Scheme 1, during tilt angle measurement the incident X-ray beam was along the x-axis, and the direction of elongation during tensile test was along the z-axis. As presented in Scheme 1, the samples were tilted at different angles (x-axis rotation at α = 0°, 36°, 60°, and 90°). Therefore, during tilt angle measurement the xz-plane was tilted with respect to the incident X-ray beam. During rotation (refer to Scheme 2), the z-axis (direction of elongation) was rotated at different angles (z-axis rotation at φ = 0°, 36°, 60°, and 90°). For z-axis rotation at φ = 0°, the xz-plane was turned and rotated compared to the position of x-axis rotation at α = 0°. Then the xz-plane was rotated at different φ-values. The scanning was performed at four positions (A_1, A_2, A_3, and A_4) along the direction of elongation (i.e., z-axis) (refer to Scheme 3). The vario-stage sample holder was used to perform this scanning experiment. Here the experimental set-up of the sample is similar to the position φ = 90°.

The 3D-tomography of the tensile-tested PBSANC sample using FIB/scanning electron microscopy (SEM) cross beam system starts by cutting 2D-slices through the selected volume by milling steps and cross-section then imaged by high-resolution scanning electron microscope (HR-SEM) (Zeiss FIB/SEM cross beam, model Auriga) [15]. Then the 2D-images were aligned using cross correlation of reference markers and finally, computer reconstruction of 2D-images enables the 3D-morphology of the dispersed silicate layers in the PBSA matrix. Around 100 images from more than 300 xy-cross sections were used for 3D-reconstructions. One of such xy-cross section profile is presented in Fig. 1(b).

For the preparation of cross sections using FIB, the Gallium ion beam was perpendicular to the sectioning plane of interest. To avoid damage, prior to the milling, the PBSACN tensile-tested sample was sputter coated using AuPd alloy for 2.5 min at 20 mA current. At first, a deep 2D-

cross-sectional surface through the sample was milled using a milling current of 4 nA. The cross-section was then polished by employing a milling current of 600 pA. After that, 600 pA current was used to cut ~30 nm thick slices.

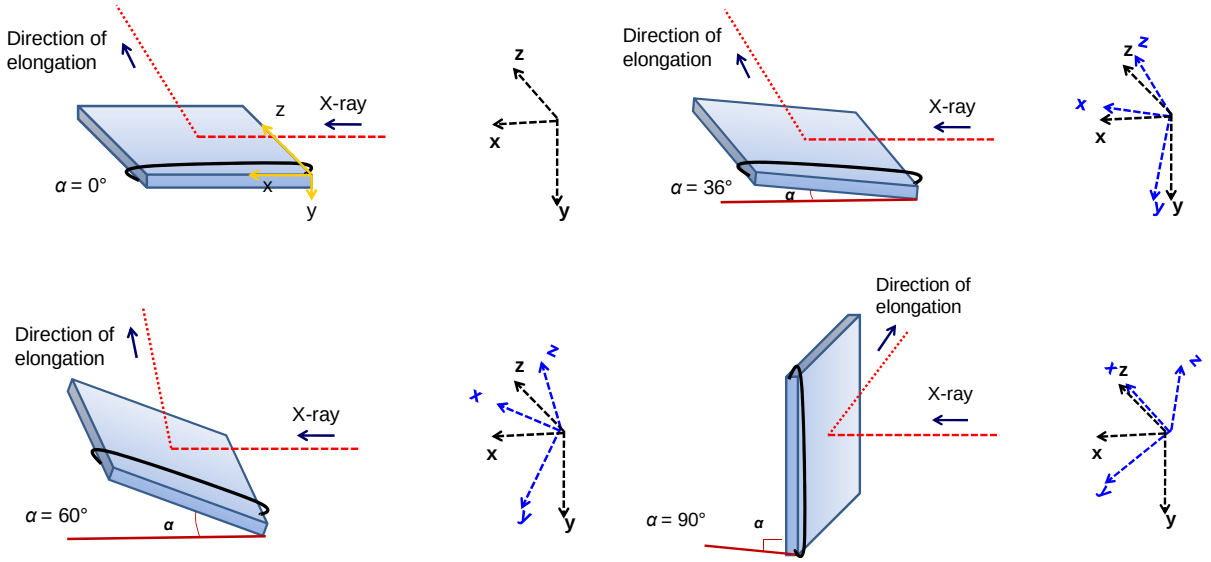

Scheme 1. Variation of tilt angles of the sample with respect to the incident X-ray beam. The sample was fixed by the black o-ring as shown in the schematic diagram.

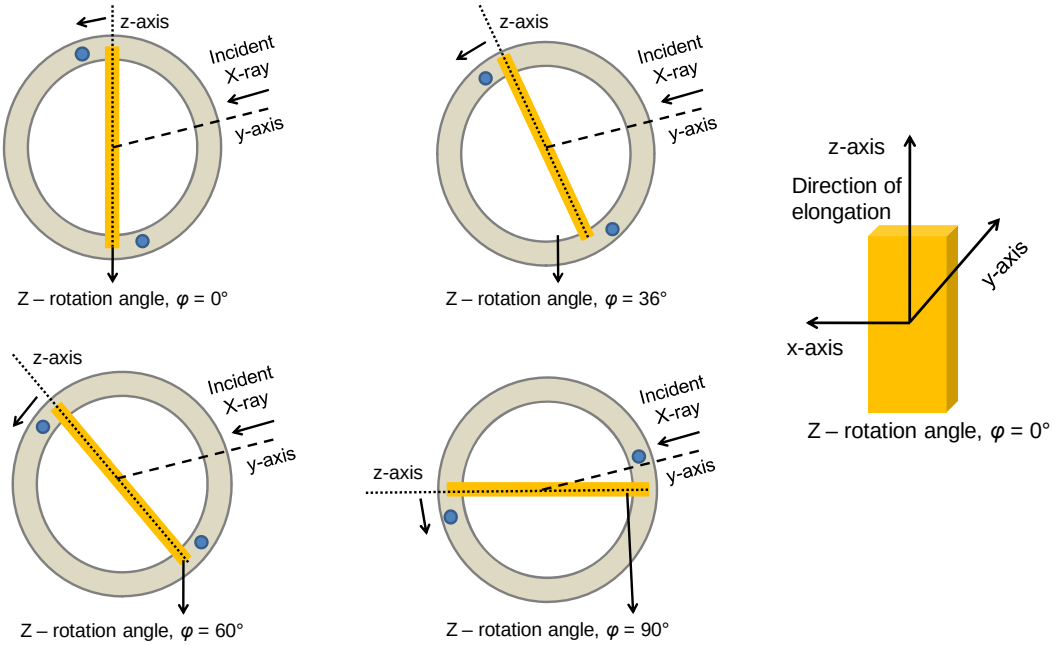

Scheme 2. Variation of rotation angles of the sample with respect to the incident X-ray beam.

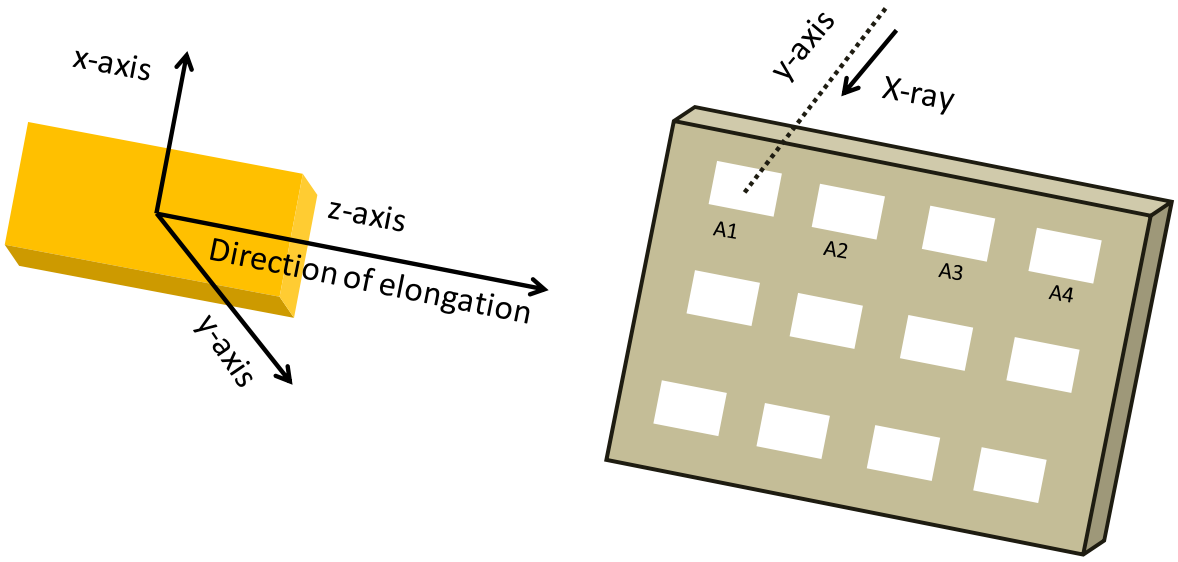

Scheme 3. Variation of scanning position with respect to the incident X-ray beam. A_1, A_2, A_3, A_4 are representing the scanning position of the sample.

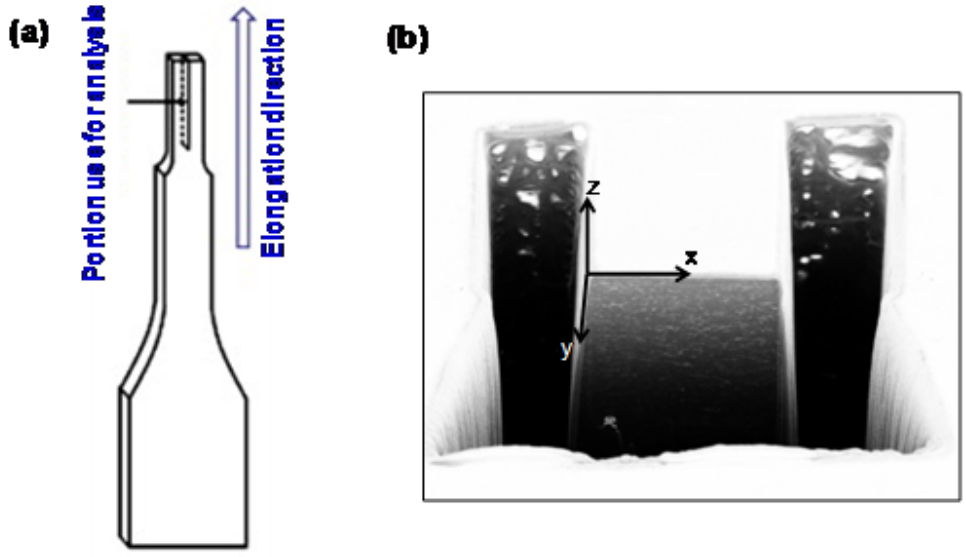

Fig. 1. (a) Portion of sample collected for analyses after tensile tests and (b) a representative highly polished scanning electron microscopic image of the xy-cross section by focused ion beam. More than 300 of such images were collected and then 100 of them were used 3D-reconstruction.

3. Results and discussion

3.1. Tilt angle measurements

3.1.1. Dispersion characteristics

To examine the effect of elongation during tensile test on the dispersion of clay platelets, the 2D-scattering patterns were analysed with pi-profile. The scattering patterns of neat polymer and composite at different tilt angles (α) are presented in parts (a) and (b) of Fig. 2, respectively. The pi-profile with contrast 53 was used to extract the scattering curves from the 2D-scattering patterns. Fig. 3 shows the normalised scattering intensity vs. scattering vector (q) plots for neat PBSA and PBSANC, in the small angle region. According to Fig. 3(a), for neat PBSA a peak appeared around 1.2 nm^{-1} at $\alpha = 0°$. This peak is due to the ordered structure of PBSA chains. During tensile testing, the PBSA chains get oriented in a certain direction and form such ordered structures. But this peak vanishes for $\alpha = 36°$ and 60°. However, it reappears again as a little hump for $\alpha = 90°$. We have reported earlier, during SAXS measurements of compression-moulded samples with line collimation geometry in the transmission mode, such humps appeared at $q = 0.5$ nm^{-1} [14]. Therefore, due to stretching during tensile test, the improvement of ordering in PBSA chains may produce such changes in peak position from 0.5 nm^{-1} to 1.2 nm^{-1}.

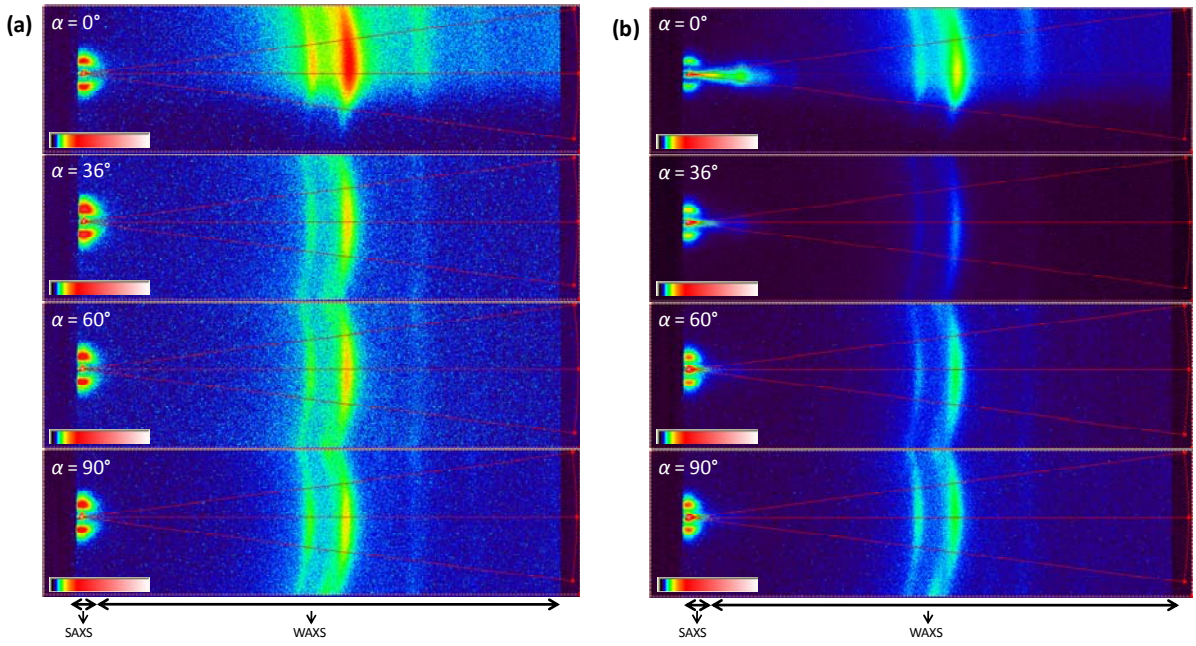

Fig. 2. 2D scattering patterns of (a) PBSA and (b) PBSANC at different tilt angles with pi-mask.

In the case of PBSANC (refer to Fig. 3(b)), a very shallow peak appeared at q = 1.6 nm^{-1} for α = 0°. The other three peaks appeared at 3.2, 4.8, and 6.4 nm^{-1}for α = 0°. The first peak appears at 1.6 nm^{-1}, second one at 3.2, third one at 4.8, and forth one at 6.4 nm^{-1}, representing the characteristic (001) clay peak with higher order clay peaks. These clay peaks are disappearing when α changes from reflectance (α = 0°) to transmittance (α = 90°). For this reason, it is difficult to find the clay peaks in transmission mode when they are very nicely dispersed. The change of tilt angle gives us information about the overall dispersion characteristics of clay platelets in the polymer matrix.

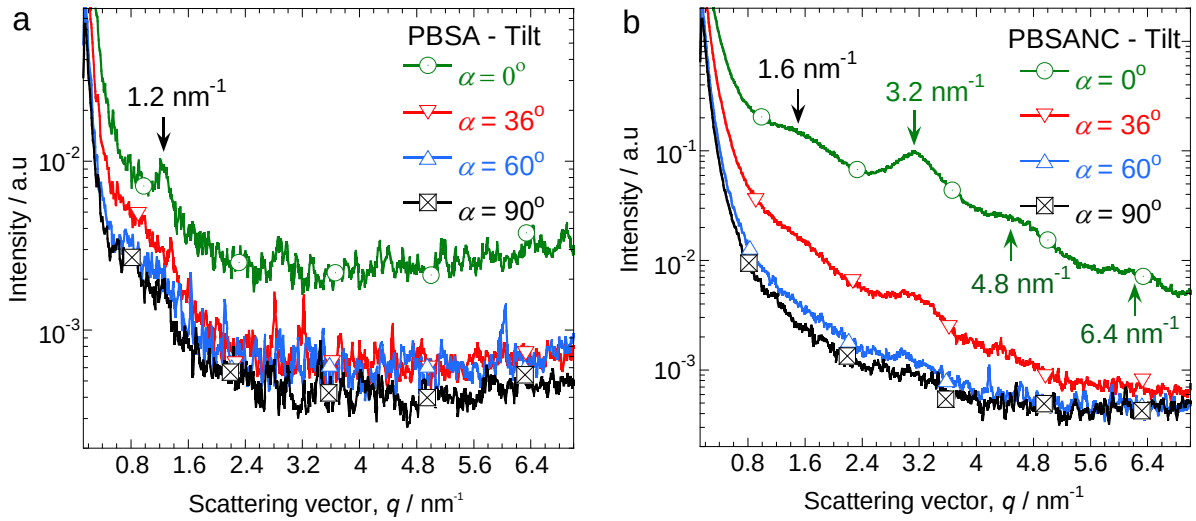

Fig. 3. Normalised scattering intensity vs. scattering vector plots for (a) PBSA and (b) PBSANC at different tilt angles in the small angle region.

To have a more detailed understanding of the dispersion characteristic of the clay platelets in the PBSA matrix, extensive structural analyses were conducted. For this purpose, the scattering profiles of neat PBSA at different α-values were taken as a background and then subtracted from the corresponding scaled intensity vs. q curves for the PBSANC. Finally, after Porod extrapolation the constant background was subtracted, and the results are presented in Fig. 4a as ift-0°, ift-36°, and so on. Now these ift-curves for different tilt angles were analysed by the Generalised Indirect Fourier Transformation (GIFT) technique (details can be found in supporting document) [13, 14]. According to this technique, the sums of the Fourier-transformed spline functions whose oscillations are restricted by Lagrange multipliers (λ_L) give an approximated scattering curve. This analysis also provides some additional information, like $p(r)$. $p(r)$ is the pair-distance distribution function of the electrons; or in other words, the radial or spherical symmetric correlation function of electron density differences weighted by $4\pi r^2$. It

shows directly the probability of finding a pair of electron density at a particular distance r. The requirements of the GIFT technique are: specification of the number of spline functions (N) and the upper limit of the largest particle dimension (D_{max}). The number of spline functions (N) used to cover the range of $p(r)$ was 20. For $\alpha = 36°$, 60°, and 90° the value of D_{max} used was 15.5 nm and for $\alpha = 0°$, the value of D_{max} used was 10.4 nm. Initially, we determined approximated scattering curve, for 19 different λ_L-values and finally, we chose a particular λ_L-value for which the approximated scattering curve is similar to the experimental scattering curve. In Fig. 4(a) 'APP' stands for approximated scattering curve. As Fig. 4(a) shows, the approximated results match nicely with the experimental scattering curve for all the tilt angles examined. Therefore, the approximated pair-distance distribution function of the electrons (e.g., GIFT-0°, GIFT-36°, etc.) from where the scattering curve was estimated should be similar to the $p(r)$ representing the experimental scattering curves (presented by e.g., ift-0°). The values of $p(r)$ of PBSANC at different tilt angles are depicted in Figs. 4 (b)-(d). The regions with opposite signs of different electron density give negative contributions to $p(r)$, i.e., $p(r)$ can be negative in some regions as observed for the case of PBSANC at $\alpha = 0°$ in Fig. 4(b). The correlation maximums (i.e., the peak positions) represent the average radial distance to the next neighbouring domain, commonly known as long spacing. Therefore at $\alpha = 0°$, in PBSANC stacked clay layers are mostly separated. With a change of tilt angles, the overlap of the clay layers due to tensile stretching becomes prominent. As a result, the $p(r)$ profile changes from $\alpha = 0°$ to $\alpha = 36°$, and so on. Therefore, according to Figs. 4(b)-(d), the PBSANC possesses some distinct neighbours when the dispersion on the surface ($\alpha = 0°$) of the sample was investigated. The tensile stretching orients the clay platelets in such a way that the clay platelets start to overlap mainly in the core of the sample.

Now in a way similar to the GIFT method, one can determine the electron density distribution profile for the dispersed clay platelets (refer to the theoretical section in supporting document as Appendix). The deconvolution (DECON) of approximated electron density distribution function provides a $p(r)$ function as denoted by e.g., DECON-0° in Fig. 4(b)-(d). If the $p(r)$ values determined by both GIFT and DECON matches nicely, one can claim the approximated electron density profile should correspond to the experimental scattering result. Since in Fig. 4(b)-(d), the $p(r)$ determined by both GIFT and DECON matches nicely, the electron density profile presented in Fig. 4(e) should represent the electron density profile for ift-curves. According to Fig. 4(e), for $\alpha = 0°$ electron density has positive and negative contributions. With an increase of the α-value, the negative contribution in the electron density profiles decreases. Such a result again confirms that the information regarding the dispersion of clay platelets in the xz-plane varies with the tilt angle of the sample with respect to the incident X-ray beam.

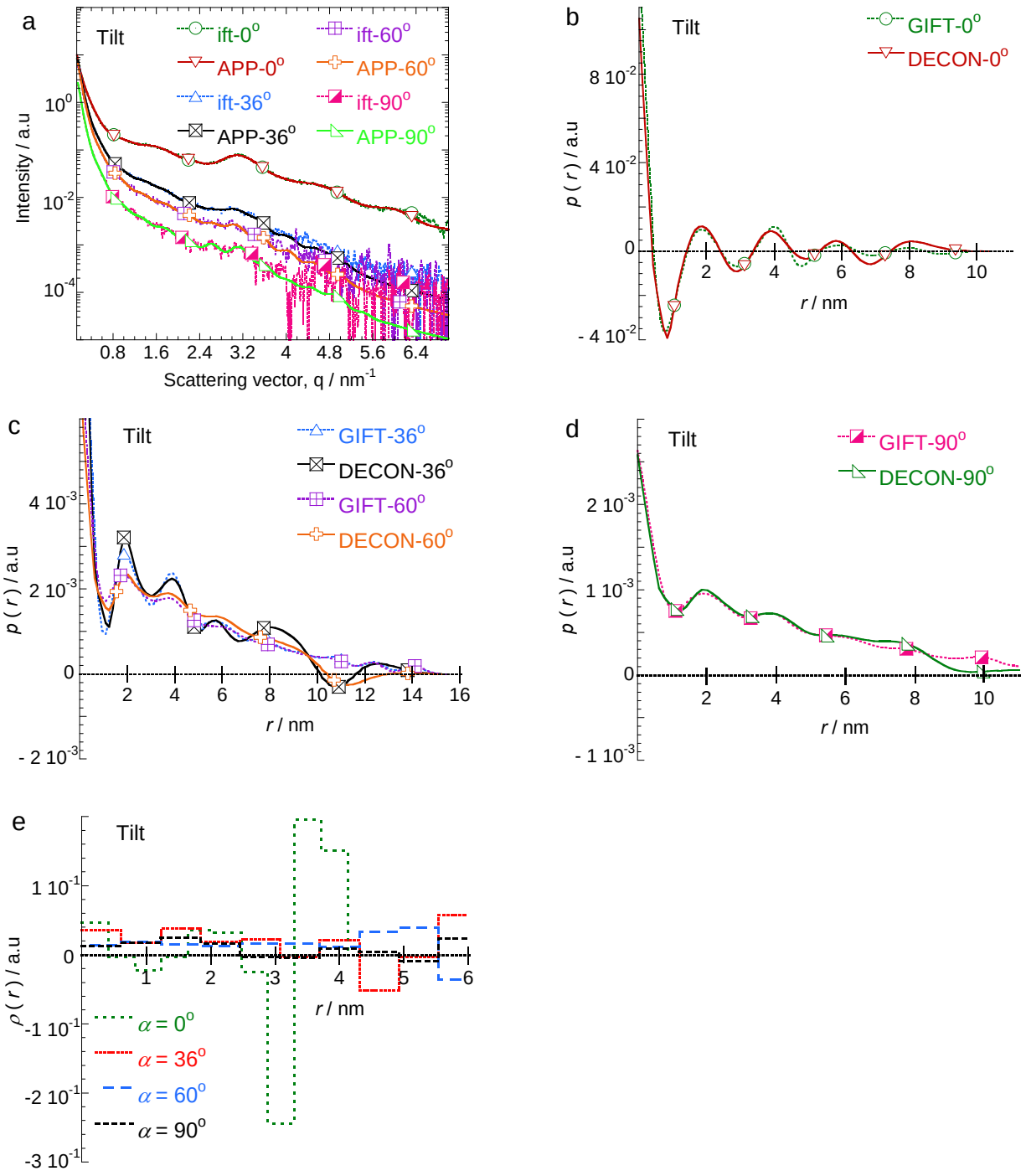

Fig. 4. (a) Background (PBSA) subtracted scattering profile of PBSANC at different tilt angles. "ift" stands for experimental scattering curve after background subtraction and "APP" stands for approximated scattering curves determined on the basis of GIFT. (b) The pair distance distribution function, $p(r)$ for PBSANC at tilt angle 0° determined on the basis of GIFT and DECON, (c) $p(r)$ for PBSANC at tilt angle 36° and 60°, (d) $p(r)$ for PBSANC at tilt angle 90°, and (e) electron density profile of PBSANC at different tilt angles determined on the basis of DECON.

3.1.2. Orientation of dispersed clay platelets

In a densely packed system of particles, the positional ordering can develop a preferential orientation with respect to each other, especially when the particles are not spherical. The degree of orientation can be detected easily from the two dimensional (2D)-SAXS patterns. Usually, the arc-profile is used to determine the orientation of crystals in a certain basal plane. Parts (a) and (b) of Fig. 5, respectively, represent the 2D-SAXS patterns of neat PBSA and PBSANC with the variation of tilt angles. Both samples after tensile test show a scattering pattern similar to the oriented sample. The scaled normalised scattering profiles (determined on the basis of the arc-mask shown in Fig. 5) against the orientation angle for both samples at different α-values are presented in Fig. 6. In order to get information on the orientation of the dispersed clay layers, the scattering profile of PBSA was subtracted from that of PBSANC. The background-subtracted scattering profiles are depicted as PBSANC-SBG in Fig. 6. Again, the degree of anisotropy (doa) and the mean orientation direction from azimuthal scattering profiles (refer Fig. 6) were estimated according to the programme "tdoa" (refer to the theoretical section in supporting document) and calculated values are presented in Table 1. According to Fig. 6 and Table 1, for all α-values, PBSA chains are oriented at an angle ~0° or 180° and the clay layers are oriented perpendicular to the polymer chains. But the intensity of the clay peak is highest at $\alpha = 0°$, and it reduces as α increases. It should be noted that the assumption used for the whole analysis was that clay platelets are infinitely long and we are considering the thickness cross-section profile of the clay platelets. Therefore, this analysis indicates, at $\alpha = 0°$ most of the thickness cross-section profiles of the clay layers get oriented perpendicular to the xz-plane as demonstrated in Fig. 7, and the polymer chains are oriented along the xz-plane. If we probe the sample along the thickness of the sample (e.g., $\alpha = 90°$) (refer to Fig. 7), only a few thickness cross-section profiles of the clay layers are there oriented parallel to the xz-plane. However, most of the clay layers are oriented perpendicular to the xz-plane. Therefore, during tensile stretching mostly on or next to the surface of the sample, clay platelets get oriented perpendicular to the xz-plane.

3.1.3. Crystalline region

Parts (a) and (b) of Fig. 8 show the normalised scattering intensity vs. scattering vector (q) plots for neat PBSA and PBSANC, respectively, in the wide angle region. According to Fig. 8(a), there are four peaks in the crystalline region of neat PBSA. These peak positions remain unaltered with the variation of tilt angles. PBSANC shows results similar to neat PBSA (refer to Fig. 8(b)). Therefore, the crystal forms of neat PBSA remain the same after preparation of nanocomposite.

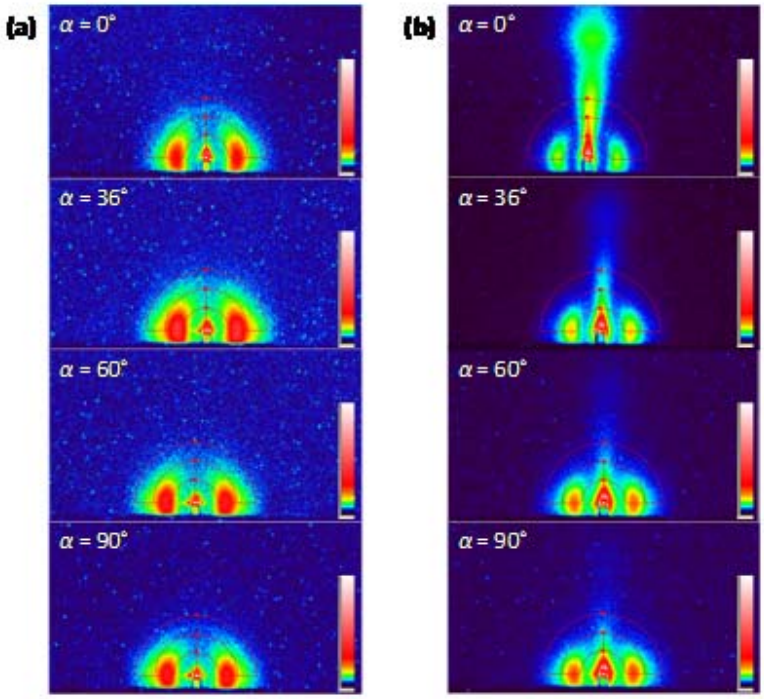

Fig. 5. 2D scattering patterns of (a) PBSA and (b) PBSANC at different tilt angles with arc-mask.

3.2. Rotation

3.2.1. Orientation of polymer chains

To obtain a more detailed understanding about the dispersion and orientation of the clay platelets in PBSANC, both neat PBSA and PBSANC samples after tensile test were characterized according to Scheme 2 (refer the Experimental procedure section). The 2D-scattering patterns were first analysed with pi-profile as demonstrated in Fig. 9. The scattering patterns of neat PBSA and PBSANC at different rotation angles (φ) extracted from these 2D-images are presented in Fig. 10. The contrast was kept the same as the tilt analysis to extract the scattering curves from the 2D-images. The normalised scattering intensity vs. q plots for neat PBSA and PBSANC in the WAXS region are presented in Fig. 11. According to Fig. 10(a), for neat PBSA a sharp peak appeared around 0.8 nm^{-1} at φ = 0°. As mentioned earlier, this peak is due to the ordered structure of PBSA chains. During tensile testing, the polymer chains get oriented in a certain direction and form such ordered structures. But the intensity of this peak decreases with increases in the value of the rotation angle from 0° to 90°. This fact suggests that most of the polymer chains get oriented in the direction depicted by φ = 0°. A similar result can be observed for PBSANC (refer Fig. 10(b)). Therefore, this rotation experiment mainly provides information on the orientation of the PBSA chains.

Now the orientation of crystals in a certain basal plane was determined by using an arc-mask for the same 2D-scattering patterns. The 2D-images with arc profile are presented in Fig. 12. In Fig. 13 the normalised scattering intensity for the masked region was plotted against the orientation angle. According to this figure it is clear that PBSANC has an intercalated structure since PBSA and clay peaks appeared alternately. Again, for all the rotation angles examined the orientation of neat PBSA and PBSANC always remained orthogonal.

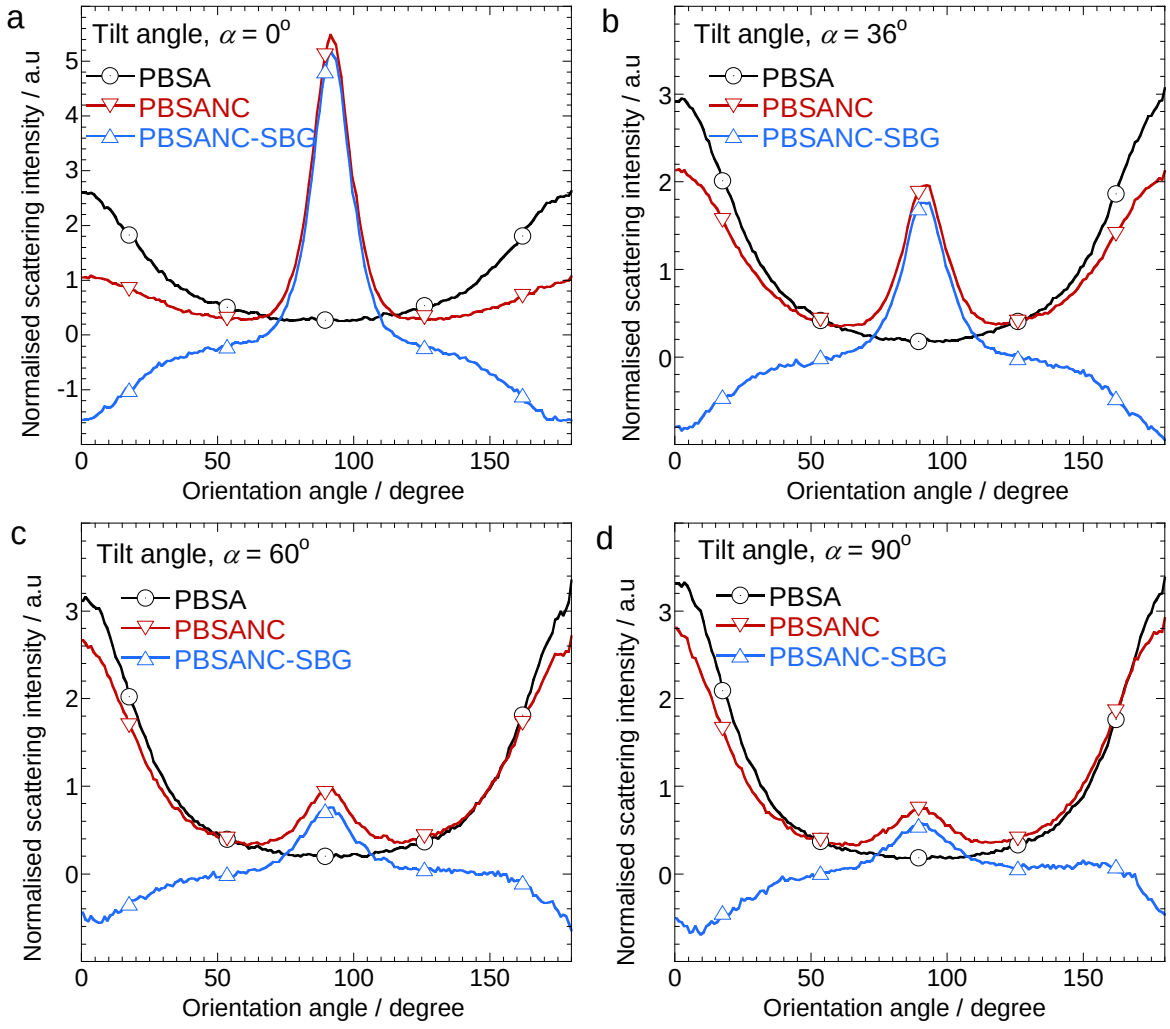

Fig. 6. Normalised scattering profiles (determined on the basis of the arc mask presented in Fig. 4) plotted against the orientation angles at different tilt angles. SBG indicates the background (PBSA) subtracted scattering profile.

Table 1. The degree of anisotropy (doa) and the mean orientation direction determined on the basis of tilt angle measurements.

Sample	Tilt angle / degree	Degree of anisotropy / %	Orientation angle / degree
	0	67.3	0
PBSA	36	70.0	0.6
	60	72.1	0.8
	90	74.7	1.5
	0	53.0	90.1
PBSANC	36	39.1	91.0
	60	29.8	94.7
	90	26.4	100.1

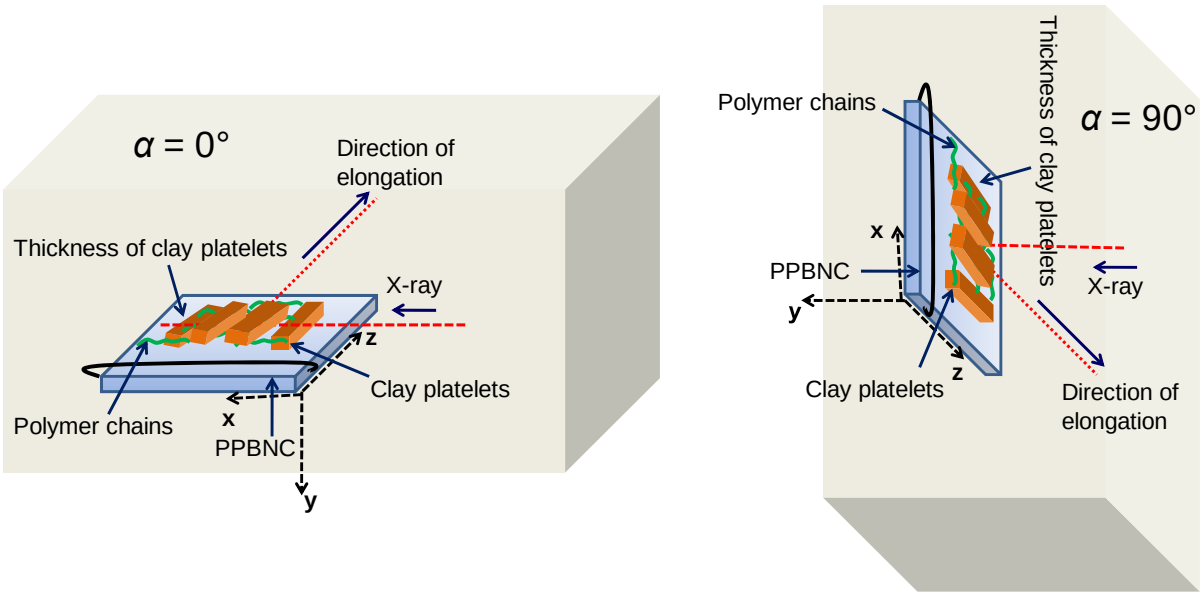

Fig. 7. Schematic representation of the orientation of polymer chains and dispersed clay layers at tilt angle 0° and 90°.

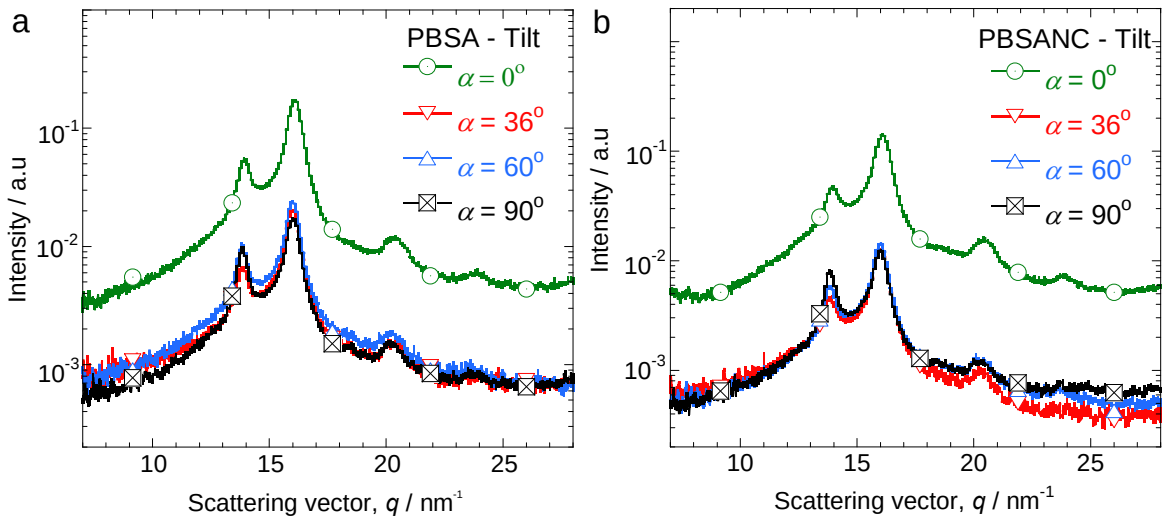

Fig. 8. Normalised scattering intensity vs. scattering vector plots for (a) PBSA and (b) PBSANC at different tilt angles in the wide angle region (determined on the basis of pi-profile).

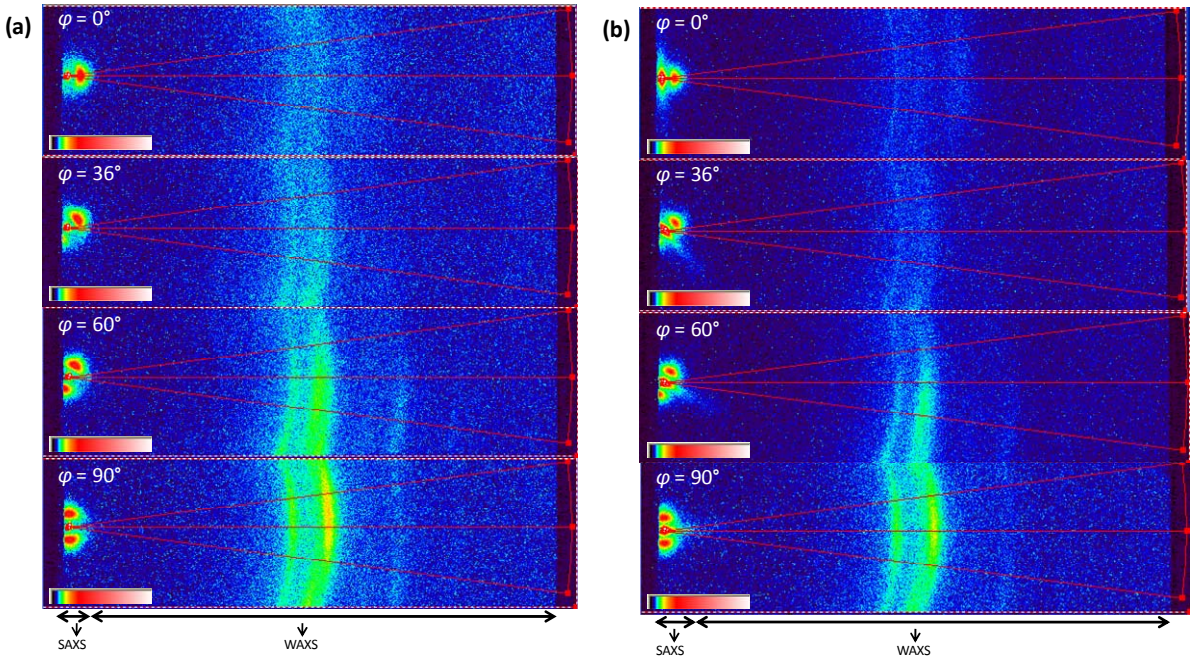

Fig. 9. 2D scattering patterns of (a) PBSA and (b) PBSANC at different rotation angles with pi-mask.

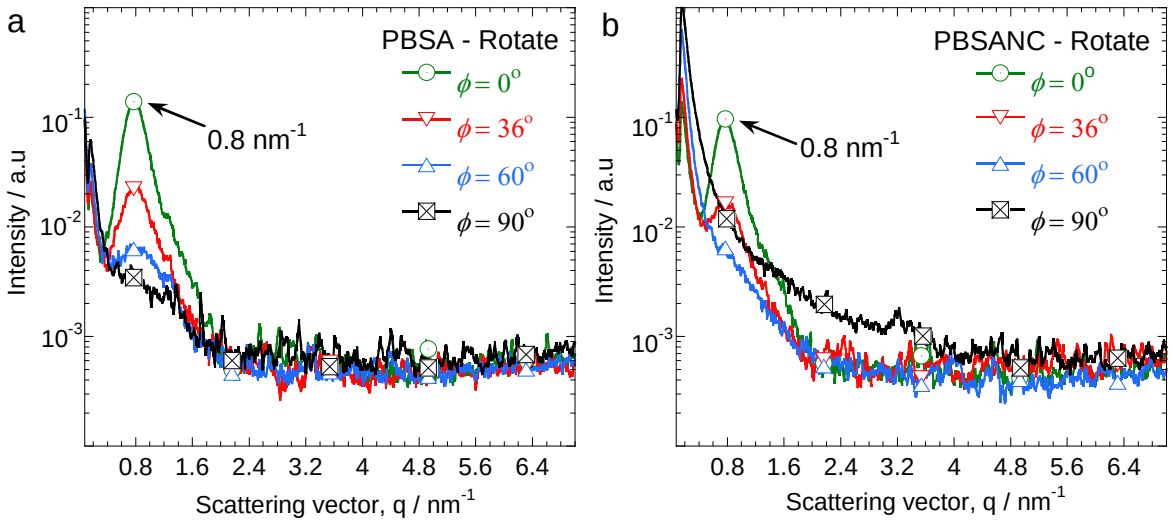

Fig. 10. Normalised scattering intensity vs. scattering vector plots for (a) PBSA and (b) PBSANC at different rotation angles in the small angle region.

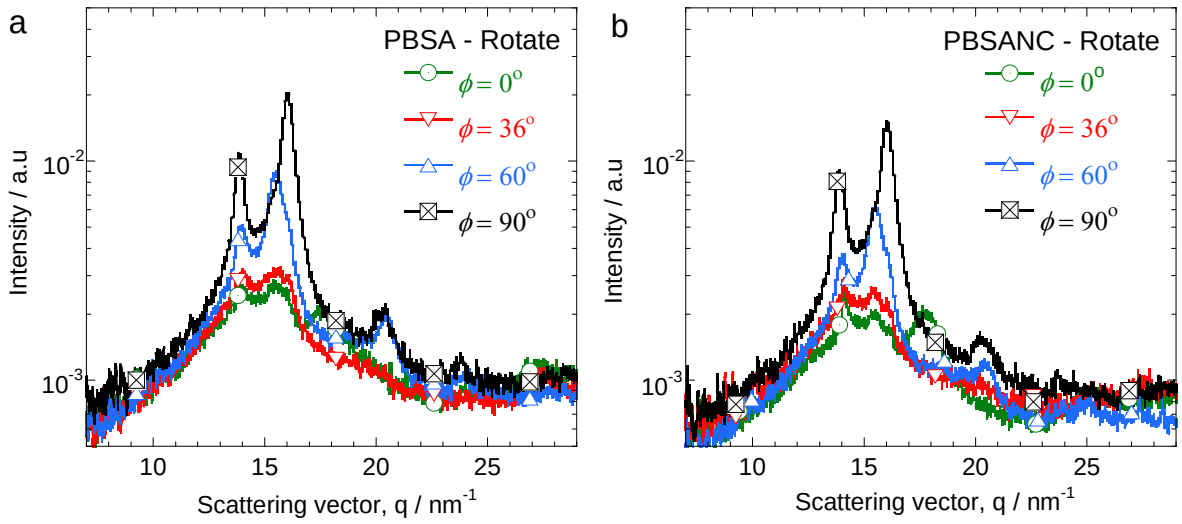

Fig. 11. Normalised scattering intensity vs. scattering vector plots for (a) PBSA and (b) PBSANC at different rotation angles in the wide angle region (determined on the basis of pi-profile).

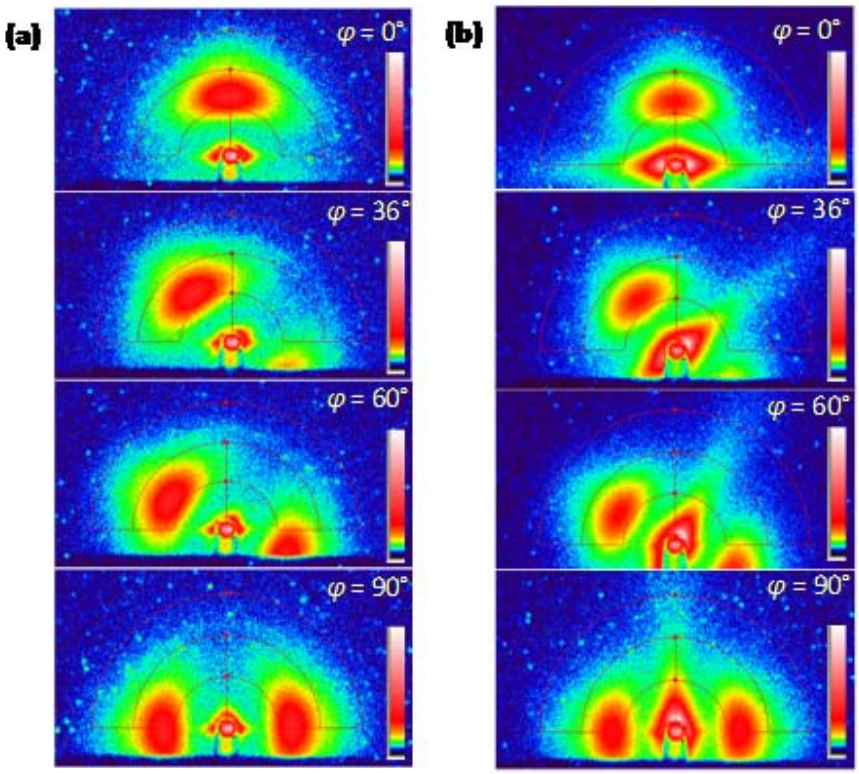

Fig. 12. 2D scattering patterns of (a) PBSA and (b) PBSANC at different rotation angles with arc-mask.

3.2.2. Crystalline region

The most important observation from this rotational test is that the intensity of polymer peak in the wide angle region increases with variation of φ from 0–90° (refer Fig. 11). However, as mentioned earlier, in the small angle region the intensity of polymer peak decreases with the variation of φ from 0–90°. It is well-known that according to the reciprocity theorem of scattering big structures scatter in the small angle side and smaller ones to the higher angle side. Therefore, the reduction of polymer peak intensity in the small angle side is attributed to the fact that the overlapping of polymer chains responsible for the ordered structure decreases when the sample was rotated from φ = 0° to 90°. In the case of PBSANC, the ordering of polymer chains can be viewed only for the position φ = 0° and 36°.

Now we can ask a very simple question: why does the intensity variation of the polymer crystal peak with change in rotation angle differ in small and wide angle regions for both samples? According to Fig. 11 the crystal peak position of neat PBSA remained unchanged after nanocomposite preparation. This indicates both samples possess the same type of crystal lattices. But the information of these crystalline planes can be obtained distinctively for φ = 90°. The reason behind this can be understood easily from the drawing presented in Fig. 14, where at φ = 0°, the X-ray probes through the xz-planes in such a way that it gets scattered from the ordered

structure of polymers and a few stacked clay layers. However, at φ = 90° the X-ray interacts more with the crystalline lattices of polymer. For this reason, the intensity of the polymer crystal peak is higher in the wide angle region at φ = 90°, but not at φ = 0°. On the other hand, the polymer peak in the small angle region, due to ordered polymer chains, becomes more prominent at φ = 0°, but not at φ = 90°.

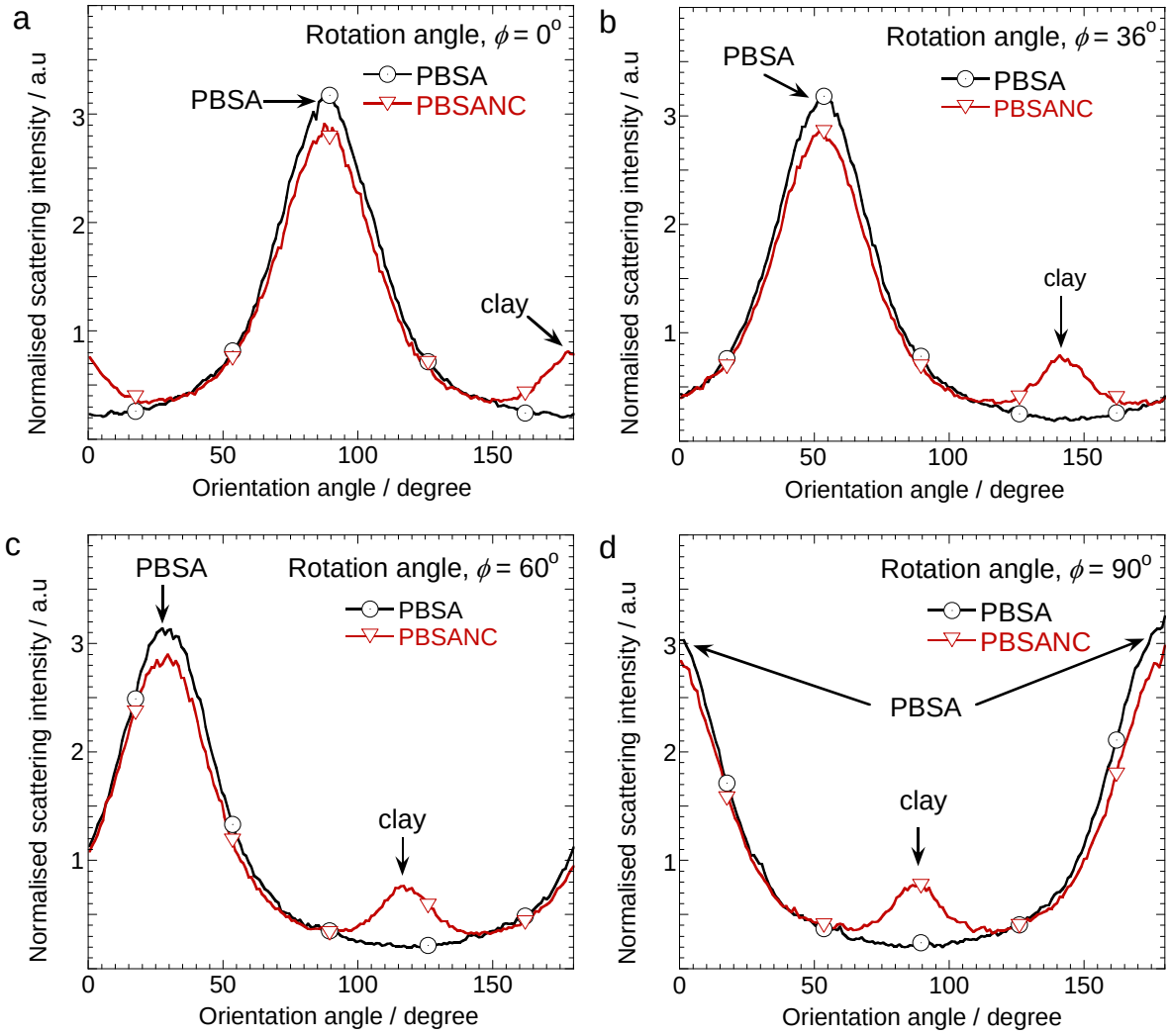

Fig. 13. Normalised scattering profiles (determined on the basis of the arc mask presented in Fig. 12) plotted against the orientation angles at different rotation angles.

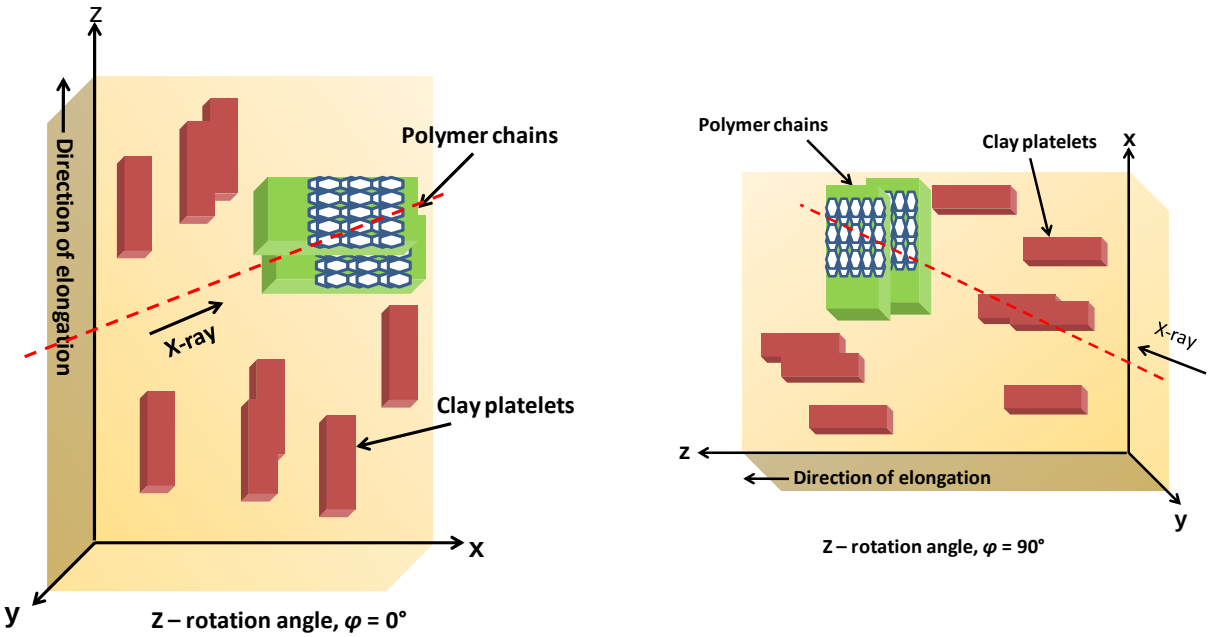

Fig. 14. Schematic representation of the orientation of polymer chains and dispersed clay layers at rotation angle 0° and 90°.

3.3. Scanning at different positions

Scanning the samples at different positions along the direction of elongation allows us to see the effect of unidirectional stretching (during tensile test) on the dispersion of clay platelets in the polymer matrix. This experiment also provides some information on the crystallinity of neat PBSA and PBSANC after tensile tests.

3.2.1. Effect of unidirectional stretching on the periodic arrangements of polymer chains and dispersed clay layers.

The 2D-scattering patterns of neat PBSA and PBSANC at different scanning positions (A_1, A_2, A_3, and A_4) with pi-profile are presented in Fig. 15. The scattering patterns of neat polymer and composite at different positions extracted from these 2D-images are shown in Fig. 16 and 17. The contrast was kept the same as in the tilt analysis to extract the scattering curves from the 2D-images. Parts (a) and (b) of Fig. 16, respectively, show the normalised scattering intensity vs. q plots for neat PBSA and PBSANC, in the small angle region. It is interesting to note that two distinctive peaks at 0.8 and 1.2 nm^{-1} appeared in Fig. 16(a), especially for scanning positions A_3 and A_4. These peaks are due to the periodic arrangements of PBSA chains in the direction of elongation. Since the positions A_3 and A_4 are closer to the stretching site, the regular arrangements of polymer chains are more prominent there. Anyway, the first crystal peak at 0.8 nm^{-1} can also be detected by the rotation experiment and the second one (at 1.2 nm^{-1}) by the tilt angle measurement. As expected, these peaks are not as sharp as the results obtained during the rotational experiment at $\varphi = 90°$.

According to Fig. 16(b), the clay peak at 3.2 nm^{-1} appeared for all the scanning positions examined. But the intensity of this peak is highest at position A_1, and it decreases as one move towards position A_4. Therefore, it is clear that the periodic arrangement or the stacking of dispersed clay layers reduces slightly near the stretching site compared to the fixed clamp site during tensile testing.

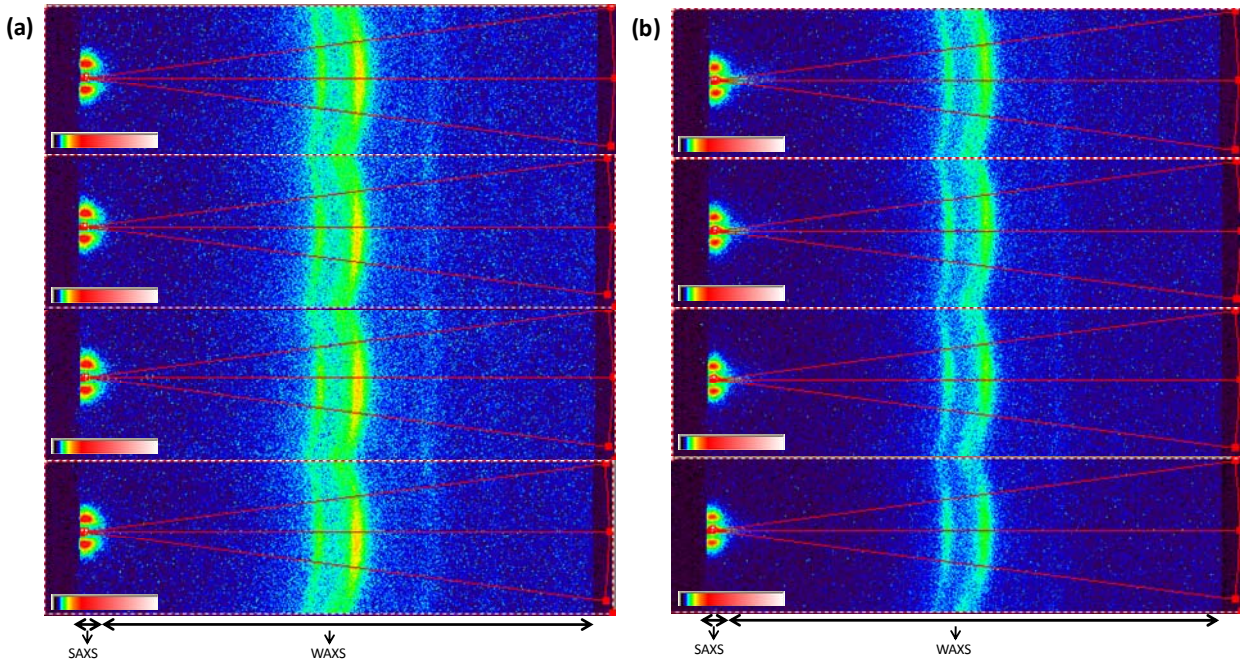

Fig. 15. 2D scattering patterns of (a) PBSA and (b) PBSANC at different scanning positions with pi-mask.

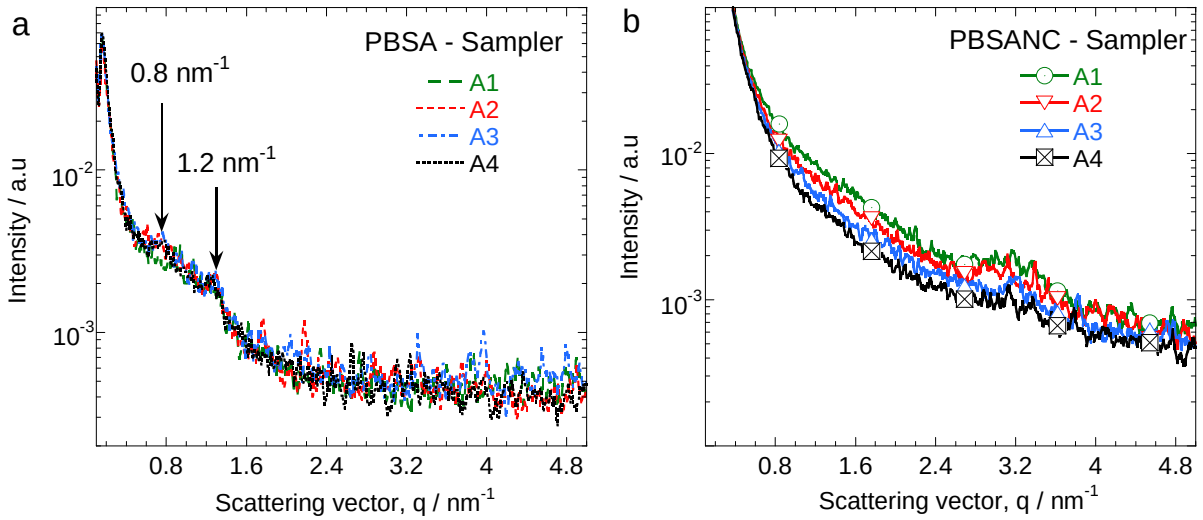

Fig. 16. Normalised scattering intensity vs. scattering vector plots for (a) PBSA and (b) PBSANC at different scanning positions in the small angle region.

3.3.2. Crystalline region

Figs. 17(a) and (b), respectively, show the normalised scattering intensity vs. scattering vector (q) plots for neat PBSA and PBSANC, in the wide angle region. According to these figures the crystal forms of neat PBSA after tensile test remained unaltered in PBSANC after tensile test. In order to estimate roughly the percent crystallinity, the area under the normalised curves were calculated within the q-value range 8–29 nm^{-1}. The estimated percent crystallinity values are tabulated in Table 2. According to this table, the percent crystallinity in PBSA after tensile test is ~5% and that in PBSANC under the same condition is ~4%. Therefore, the percent crystallinity decreases slightly in PBSANC. Because of the even dispersion of the clay platelets in the PBSA matrix, the overall crystal growth gets hampered [16] and as a result, the percent crystallinity decreases slightly. Usually, the decrease in crystallinity is inversely proportional to the biodegradability [17]. Therefore, it is expected from this SWAXS result that biodegradability should increase slightly in PBSANC compared to the neat PBSA.

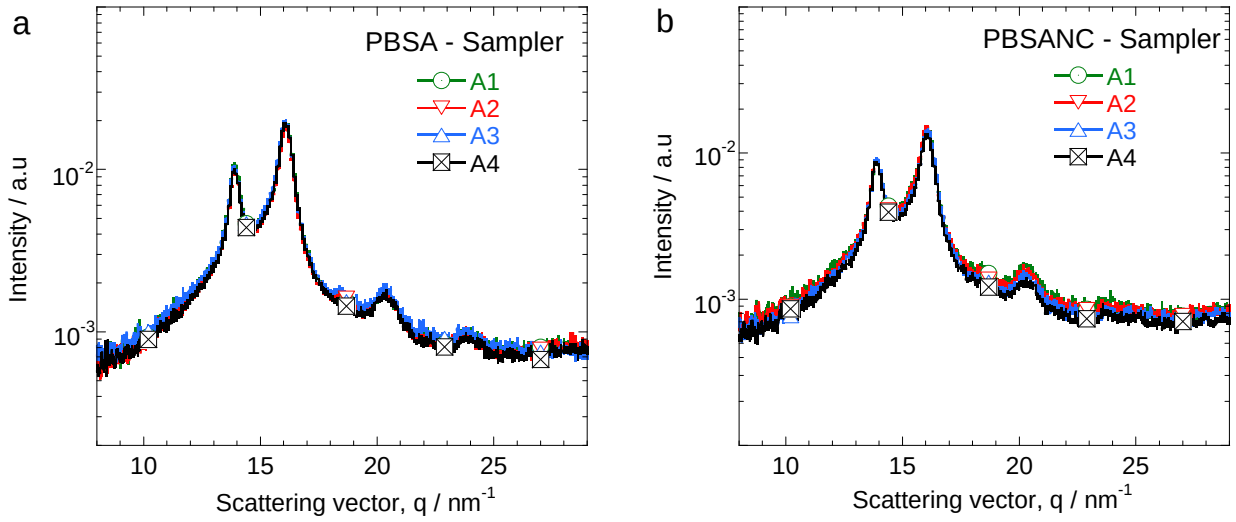

Fig. 17. Normalised scattering intensity vs. scattering vector plots for (a) PBSA and (b) PBSANC at different scanning positions in the wide angle region (determined on the basis of pi-profile).

3.4. Structural characterisation by focus ion beam electron tomography

In order to support the conclusions drawn on the basis of SWAXS analyses (especially Figs. 7 and 14), FIB-electron tomography was employed. The 3D-reconstruction from the cross-sectional images provides the information of dispersion and orientation of clay platelets in the PBSA matrix. The 3D-reconstructed images at different planes of PBSANC sample (after tensile

tests) are presented in Fig. 18. The first observation on the basis of this figure is that the dispersed clay platelets are oriented along the z-axis, i.e., the direction of elongation during the tensile test. The second observation is that the thicknesses of the clay layers are in xy- and yz-planes. The surface of the clay platelets are in the xz-plane.

Therefore, Fig. 18 strongly supports the models on the dispersion and orientation of clay platelets proposed on the basis of SWAXS analyses (Figs. 7 and14). But SWAXS studies provide extra information on the crystal planes of polymer, ordered structure of polymer chains, and also the percent crystallinity.

Table 2. Estimated percent crystallinity in PBSA and PBSANC after tensile test.

Sample	Scanning position	Percent crystallinity / %
PBSA	A_1	4.98
	A_2	4.70
	A_3	5.06
	A_4	4.72
PBSANC	A_1	4.44
	A_2	4.37
	A_3	4.13
	A_4	3.85

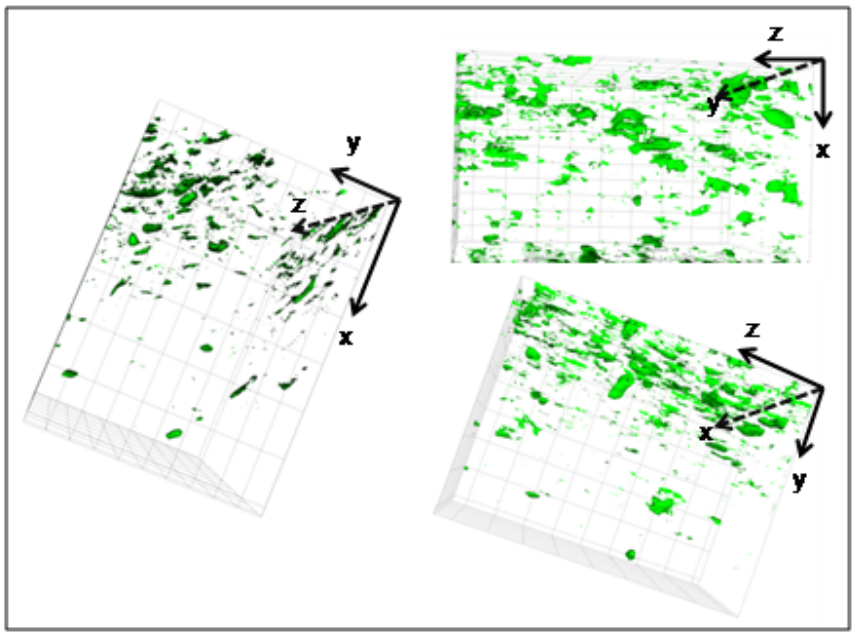

Fig. 18. The 3D-reconstructed images at different planes of the PBSANC sample by focused ion beam scanning electron microscope.

4. Conclusions

This work reports on the dispersion characteristics and orientation of clay platelets in a polymer nanocomposite after tensile test, the ordered structure of polymer chains, and their crystallinity. All these aspects were analysed using SWAXS by tilting, rotating, and scanning the samples at different planes and supported by FIB-tomography studies. Results show that the clay platelets dispersed in PBSA matrix get oriented in the direction of elongation during tensile test and the PBSA chains get oriented orthogonally to the clay layers. However, tilting the sample at different angles with respect to the incident X-ray beam provides more information on the dispersion and the orientation of clay layers, which are delaminated in PBSA matrix. The rotation of samples at different angles with respect to the incident X-ray beam provides information on the ordered arrangement in PBSA chains and also on the crystal planes. On the other hand, scanning samples at different positions allows estimating the percent crystallinity present in the sample. The FIB-tomography results support the conclusions drawn on the basis of tilt angle measurements. However, the rotation and scanning measurements provide extra information on the crystal planes of polymer chains, their ordered structure, and crystallinity.

Acknowledgement: The authors would like to thank DST and CSIR for financial support.

Supporting information available: Text discussing the theoretical background of small-angle scattering.

References

[1] Sinha Ray S, Okamoto M. Polymer/layered silicate nanocomposites: a review from preparation to processing. Prog Polym Sci 2003; 28: 1539–646.

[2] Pavlidou S, Papaspyrides CD. A review on polymer-layered silicate nanocomposites. Prog Polym Sci 2008; 33: 1119–98.

[3] Paul DR, Robeson LM. Polymer nanotechnology : nanocomposites. Polymer 2008; 49: 3187–204.

[4] Sinha Ray S, Bousmina M. Biodegradable polymers and their layered silicate nanocomposites: in greening the 21st century materials world. Prog Mater Sci 2005; 50: 962–79.

[5] Darder M, Aranda P, Ruiz-Hitzky E. Bionanocomposites: a new concept of ecological, bioinspired, and functional hybrid materials. Adv Mat 2007; 19: 1309–19.

[6] Alexandre M, Dubois P. Polymer-layeres silicate nanocomposites : preparation, properties, and use of a new class of materials. Mater Sci Eng 2000; R28: 1–63.

[6] Lloyd SM, Lave LB. Life cycle economic and environmental implications of using nanocomposites in automobiles. Environ Sci Eng 2003; 37: 3458–66.

[7] Okada A, Usuki A. Twenty years of polymer-clay nanocomposites. Macromol. Mater Eng 2006 ;291 : 1449–76.

[8] Nikolic MS, Djonlagic J. Synthesis and characterization of biodegradable poly[(butylene sucinate(-co-adipate]. Polym Degrad Stab 2001; 74: 263–70.

[9] Fujimaki T. Processability and properties of aliphatic polyesters, 'BIONOLLE', synthesized by polycondensation reactions. Polym Degrad Stab 1998; 59: 209–14.

[10] Ishioka D. Biopolymers, polyesters III. Applications and Commercial Products, Vol. 4. Weinheim: Wiley-VCH Verlag Gmbh; 2002. p. 275.

[11] Sinha Ray S, Bousmina M. Poly(butylene succinate-co-adipate)/montmorillonite nanocomposites: effect of organic modified miscibility on structure, properties, and viscoelasticity. Polymer 2005; 46: 12430–9.

[12] Sinha Ray S, Bousmina M. Structure and properties of nanocomposites based on poly(butylene succinate-co-adipate) and organically modified montmorillonite. Macromol Mater Eng 2005; 290: 759–68.

[13] Bandyopadhyay J, Sinha Ray S. Mechanism of enhance tenacity in a polymer nanocomposite small-angle X-ray scattering and electron microscopy. Polymer 2010; 51: 4860–6.

[14] Bandyopadhyay J, Sinha Ray S. The quantitive analysis of nano-clay dispersion in polymer nanocomposites by small-angle X-ray Scattering. Polymer 2010; 51: 1437–49.

[15] Sinha Ray S. A new possibility of microstructural investigation of clay-based nanocomposites by focused-ion-beam tomography. Polymer 2010 ; 51 :3966–70.

[16] Sinha Ray S, Bousmina M. Crystallization behaviour of poly[(butylene succinate)-co-adipate] nanocomposite. Macromol Chem Phys 2006; 207:1207–19.

[17] Tokiwa Y, Calabi BP, Ugwu CU, Aiba S. Biodegradability of plastics. Int J Mol Sci 2009 ;10 :3722–42.

Supporting Document [online publication only]

Theoretical Background of Small-Angle X-ray Scattering

Submitted to POLYMER

The study of dispersion and orientation of clay platelets in a polymer nanocomposite using variostage small angle X-ray scattering

Jayita Bandyopadhyay[1], Thomas Malwela[1], and Suprakas Sinha Ray[1,2] *

[1]*DST/CSIR NIC, National Centre for Nano-Structured Materials, Council for Scientific and Industrial Research, Pretoria 0001, South Africa*

[2]*Department of Chemical Technology, University of Johannesburg, Doornfontein 2018, Johannesburg, South Africa*

---

* Corresponding author. E-mail: rsuprakas@csir.co.za

1. The Relationship between Bragg condition and reciprocal lattice

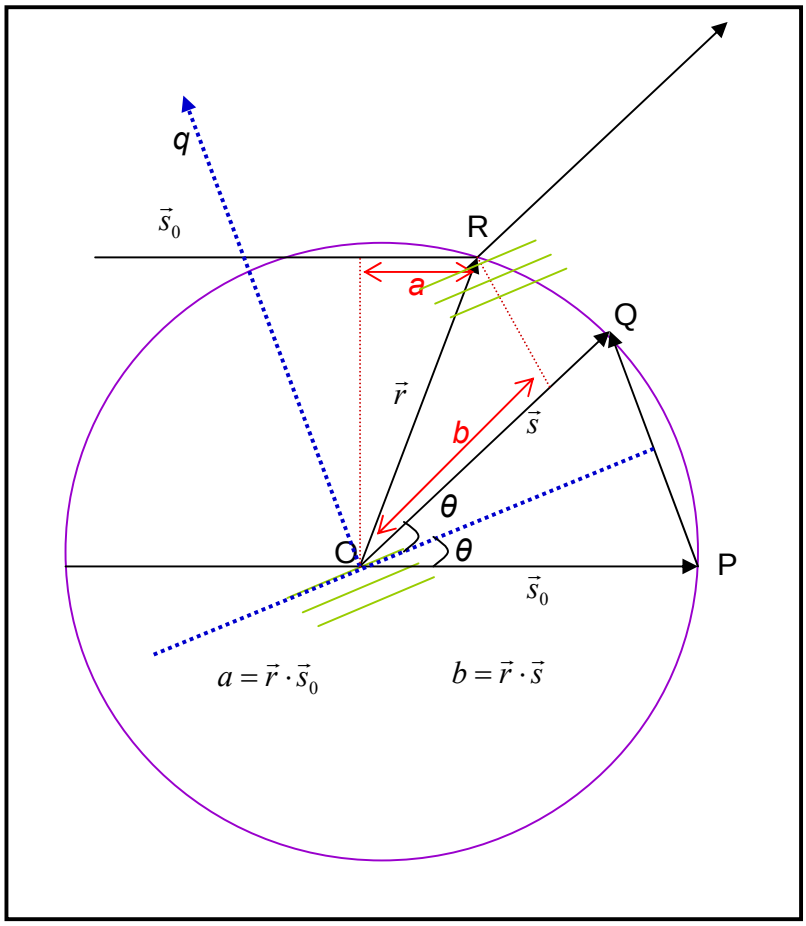

Fig. 1 The relationship between the Bragg condition and reciprocal lattice determined on the basis of Ewald sphere.

The small angle X-ray scattering (SAXS) is a powerful tool used to determine the size, shape, and internal structure of the particle system of sizes ranging from 1 to 100 nm. The SAXS analysis is mainly applicable for randomly oriented and statistically distributed particle systems. Hence, their three-dimensional scattering pattern represents the orientational average of their structure. Only in the case of three types of ideal symmetries; i.e., for spherical, cylindrical, and lamellar structures with a centrosymmetric scattering length density distribution, there is no loss of information due to the orientational averaging [1].

The scattered waves are usually coherent. Although some incoherent scattering (Compton) is also present, it can be neglected since only small angles are involved in our study. Coherence means the intensity can be obtained by the absolute square of the sum of the amplitudes. The amplitudes remain same in magnitude for all the scattered waves; however there exists a phase

difference which depends on the position of electrons in space. Conventionally, a single secondary wave can be represented by $e^{-i\varphi}$; where the phase φ is $(2\pi/\lambda)$ times the path difference. Now let's use the concept of a Ewald sphere where one particle is located at the centre O and another at position R. Usually, the relationship between the Bragg condition and reciprocal lattice can be explained by Ewald sphere. The incident beam is represented by a unit vector s_0 and scattered beam by s. According to Fig. 1, the path difference is

$$b - a = r.s - r.s_0 = r.(s - s_0) \tag{1}$$

Now according to Fig. 1,

$$(s - s_0) = 2\sin\theta \tag{2}$$

Where, 2θ is the scattering angle.

Hence the phase difference is,

$$\frac{2\pi}{\lambda} r \cdot (s - s_0) = r.\frac{4\pi}{\lambda}\sin\theta = rq \tag{3}$$

The vector q is known as reciprocal lattice vector and is perpendicular to the plane of the particle from where the scattering is taking place. Therefore, a single secondary wave can be represented by $e^{-i\varphi} = e^{-iqr}$.

Now the total scattered field ($E_s(q)$) can be obtained by integrating over whole illuminated scattering volume (v),

$$E_s(q) = const \int_v \rho(r) e^{-iqr}\, dr \tag{4}$$

The electron density $\rho(r)$ can be expressed in terms of its mean value ($\overline{\rho}$) and its fluctuation $\Delta\rho(r)$ as,

$$\rho(r) = \overline{\rho} + \Delta\rho(r) \tag{5}$$

The Fourier integral is linear, so equation (4) can be rewritten as,

$$E_s(q) = const\left[\int_v \overline{\rho}(r) e^{-iqr}\, dr + \int_v \Delta\rho(r) e^{-iqr}\, dr\right] \tag{6}$$

The integration containing the term $\overline{\rho}$ over the total volume acts as a homogeneous object and much too large to make any contribution to the diffraction pattern. Hence, this term drops out right from the beginning. Then $E_s(q)$ reduces to,

$$F(q) = \int_v \Delta\rho(r) e^{-iqr} dr \tag{7}$$

The intensity is given by the square of the amplitude,

$$I(q) = |F(q)|^2 = F(q).F^*(q) = const \int_v \int_v \Delta\rho(r_1)\Delta\rho(r_2) e^{-iq(r_1 - r_2)} dr_1 dr_2 \tag{8}$$

Substitute $r_2 = r_1 - r$ and introduce the convolution square or auto correlation function defined by,

$$\gamma(r) \equiv \Delta\tilde{\rho}^2(r) = \int_v \Delta\rho(r_1)\Delta\rho(r_1 - r) dr_1 \tag{9}$$

where, $r = (r_1 - r_2)$ = constant

The auto correlation function is calculated by shifting the ghost particle by a vector r and integrating the overlapping volume (since it is necessary to average over all possible direction in space).

Then equation (8) reduces to,

$$I(q) = |F(q)|^2 = const \int_v \gamma(r) e^{-iqr} dr \tag{10}$$

Now there are two restrictions in the small angle X-ray scattering,

(*i*) The system is statistically isotropic. It makes no difference here whether this is a property of the structure itself or a consequence of change of time (like rotation of particles).

(*ii*) There exists no long range order; i.e., there is no correlation between the two points separated wide enough.

The orientation average of $I(q) = |F(q)|^2 = const \int_v \gamma(r) e^{-i\vec{q}\cdot\vec{r}} dr$ is calculated according to Debye (in spherical coordinates)

$$\langle I(q) \rangle_{orientations} = const \int_v \gamma(r) \langle e^{-i\vec{q}\cdot\vec{r}} \rangle_{orientations} dr$$

$$\langle e^{-i\vec{q}\cdot\vec{r}} \rangle_{orientations} = \frac{1}{4\pi} \int_0^{2\pi} d\varphi \int_0^{\pi} e^{-i\vec{q}\cdot\vec{r}} \sin\theta \cdot d\theta$$

with $\vec{q} = q(0,0,1)$, $\vec{r} = r(\sin\theta\cos\varphi, \sin\theta\sin\varphi, \cos\theta)$, $\vec{q}\cdot\vec{r} = qr\cos\theta$

$$\langle e^{-i\vec{q}\cdot\vec{r}} \rangle_{orientations} = \frac{1}{4\pi} \int_0^{2\pi} d\varphi \int_{-1}^{1} e^{-iqr\cos\theta} \cdot d\cos\theta = \frac{e^{-iqr} - e^{iqr}}{-2iqr} = \frac{\sin qr}{qr}$$

Now replace $const\int_{v} d\vec{r} = 4\pi\int_{0}^{\infty} r^2 dr$ and $p(r) = r^2\gamma(r)$ in order to obtain

$$I(q) = 4\pi\int_{0}^{\infty} p(r)\frac{\sin qr}{qr}dr \qquad (11)$$

where q is the scattering vector and can be related to the scattering angle (θ) and wavelength (λ) by equation (12).

$$q = \frac{4\pi}{\lambda}\sin\theta \qquad (12)$$

The $p(r)$ in equation (3.11) represents a pair-distance distribution function of the electrons; or in other words, the radial or spherical symmetric correlation function of electron density differences weighted by $4\pi r^2$. It shows directly the probability of finding a pair of electron densities at a particular distance r. All the information available from the experimental curves in the small angle region is in reciprocal space since $q \alpha 1/\lambda$. Therefore, it is difficult to get direct information about the form and structure factors of the particles.

2. The form and structure factors

The form and structure factors can be explained as follows: Let us consider a composite particle consist of sub-particles with a fixed orientation. The positioning of the centres of mass of the sub-particles may be designated by $r_1, r_2 \ldots r_j \ldots\ldots r_N$. The scattered wave's amplitudes from these sub-particles can be designated by (with respect to each centre) $F_1, F_2 \ldots\ldots, F_j \ldots\ldots, F_N$. The positions of the sub-particles are each accounted for by an additional phase factor e^{-iqr_j}. Therefore, the total amplitude of the composite particle is

$$F(q) = \sum_{1}^{N} F_j(q).e^{-iqr_j} \qquad (13)$$

In general, each amplitude will have a phase too,

$$F_j = \left|F_j\right|.e^{i\varphi_j} \qquad (14)$$

Then the intensity is

$$I(q) = FF^* = \langle\sum_{j=k}\sum F_j F_k^*.e^{-iq\left(r_j - r_k\right)}\rangle + 2\langle\sum_{j\neq k}\sum\left|F_j\right\|F_k\left|\cos(qr_{jk} + q_k - q_j\right\rangle \qquad (15)$$

The double sum contains N terms with $j=k$, the phase factor consequently vanishing. The remaining term with $j\neq k$ represent the interference between the sub-particles according to the

relative distance $r_{jk} = (r_j - r_k)$. Since each pair is counted twice with $r_{jk} = - r_{kj}$, only the real part is accountable. Therefore, the intensity contribution with $j=k$ can be considered as form factor and that with $j \neq k$ can be considered as structure factor.

3. The Generalized Indirect Fourier Transformation method (GIFT)

The real space transformation of the SAXS data (after desmearing) by inverse Fourier transformation (IFT) of the Fredholm integral equation (see equation (11)) can determine the parameters such as *p(r)*; from where the form factor and structure factor can be evaluated. But doing IFT is impossible here because of the termination effect of *q*-scale and the influence of a remaining background scattering. These may cause some strong artificial oscillations ("Fourier ripples") in the *p(r)* function and make the analysis useless [2, 3]. At small *q*-values the measurement is limited by the unscattered primary beam and at large *q*-values by the progressive decrease of the signal-to-noise ratio. The scattered intensity is usually determined at discrete points. According to the counting statistics, the standard deviation of each data point is equal to the square root of the number of pulses registered by the counter. The termination effect can be reduced by the extrapolations of the scattering curve. For example, the Guinier approximation can be used to extrapolate the scattering curve toward a zero angle provided the first data point is measured at a very small angle. The extrapolation toward a large angle can sometimes be performed with Porod's law. But the termination effect can be minimized by the indirect Fourier transformation method developed by Glatter [4-6]. In most cases researchers are interested in studying the structure of particles dispersed in solution and to avoid background scattering the solvent is taken as a background, and then the $I(q)$ of the solvent is subtracted from the $I(q)$ of the solution. In the case of polymer nanocomposite, in order to get information about the dispersed nanoparticles, the pure polymer should be taken as a background and subtracted from the scattering intensity of the nanocomposite. The indirect Fourier Transformation takes into account the following factors: single-step procedure, optimized general function system, weighted least square approximation, error propagation, minimization of the termination effect, and consideration of the physical smoothing condition given by the maximum intra-particle distance [7]. Therefore, for smoothing conditions it is necessary to estimate the upper limit of the largest particle dimension, i.e. D_{max}. Therefore, if

$$r \geq D_{max}, \quad p(r) = 0 \tag{16}$$

Now, a function system should be defined in the range $0 \leq r \leq D_{max}$ and a linear combination of these functions should provide the *p(r)*. Therefore,

$$p_A(r) = \sum_{\upsilon=1}^{N} c_\upsilon \varphi_\upsilon(r) \tag{17}$$

where the suffix "*A*" denotes only that this *p(r)* is approximated. *N* is the number of functions and should be chosen sufficiently in order to cover the range $0 \leq r \leq D_{max}$; c_υ is an unknown and can be determined by a weighted least square approximation of the experimental data. $\varphi_\upsilon(r)$ are chosen as cubic *B*-spline functions, and they can be defined as multiple convolution products of a step function, representing curves with a minimum second derivative. Each individual spline

function can be subjected to Fourier transformation (T_1), wavelength integral (T_2), slit-length integral (T_3), and slit-width integral (T_4). The intermediate result after Fourier transformation of all the splines represents the scattering intensity without the collimation effect corresponding to a distance distribution $\varphi_\upsilon(r)$. Therefore, the intensity without the collimation effect [$\Psi_\upsilon(q)$] can be expressed as

$$\Psi_\upsilon(q) = T_1\varphi_\upsilon(r) \tag{18}$$

The smeared intensity (i.e., after adding the collimation effect) can be obtained after execution of T_2, T_3, and T_4 as

$$\chi_\upsilon(q) = T_4T_3T_2\Psi_\upsilon(q) = T_4T_3T_2T_1\varphi_\upsilon(r) \tag{19}$$

So $\chi(q)$ represents the approximated scattering data from a particle with maximum distance, D_{max}. The next step is the stabilization of these coefficients. The stabilized least squares condition is given below

$$L + \lambda_L N_{c'} = \text{minimum} \tag{20}$$

$$\text{with } L = \frac{\int_{q_1}^{q_2} [I_{\exp}(q) - \sum_{\upsilon=1}^{N} c_\upsilon \chi_\upsilon(q)]^2}{\sigma^2(q)} dq \tag{21}$$

$$\text{and } N_{c'} = \sum_{\upsilon=1}^{N-1} (c_{\upsilon+1} - c_\upsilon)^2 \tag{22}\backslash$$

Here, q_1 and q_2 are the first and last data points, $I_{exp}(q)$ is the experimental intensity, σ^2 is the estimated variance of the observed intensity, and λ_L is known as the stabilization parameter or Lagrange multiplier [2, 4, 5]. The optimum fit to the observed data points is given by

$$I_A(q) = \sum_{\upsilon=1}^{N} c_\upsilon \chi_\upsilon(q) \tag{23}$$

$I_A(q)$ represents the approximated scattering curve, which should be similar to the experimental curve, $I_{exp}(q)$. Therefore, it can be concluded that the approximated distance distribution function [$p_A(r)$] represents the $p(r)$ for the experimental curve.

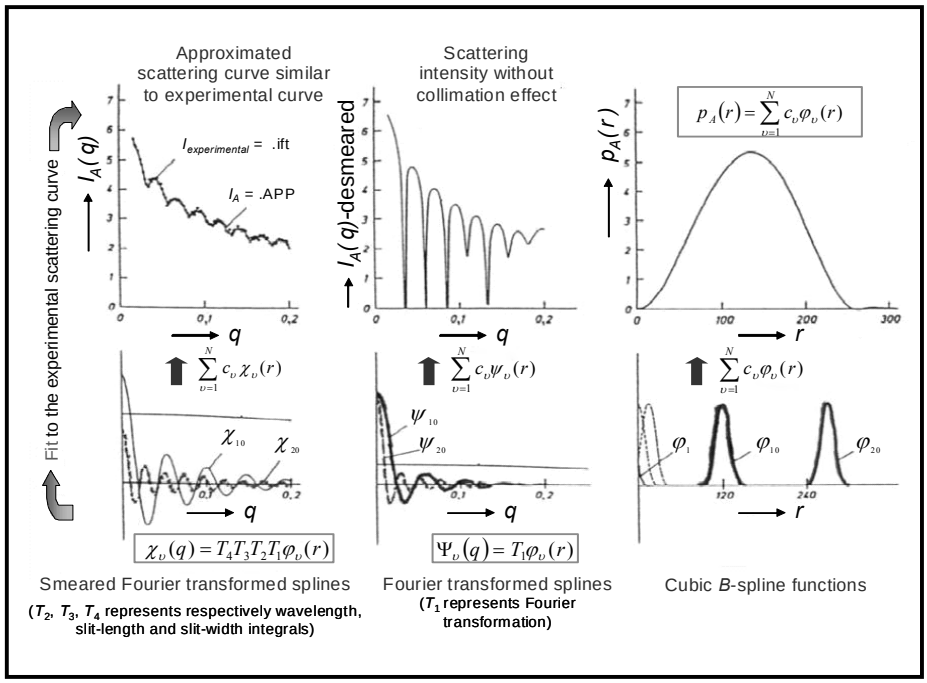

Fig. 2 The representative diagram of generalized indirect Fourier transformation (GIFT) method for spherical particle

In this study, we used the GIFT method to evaluate the *p(r)*, which is consistent with the experimental scattering curve. Fig. 2 is the representative diagram of GIFT method for spherical particle. Here we consider $p(r)$ consists of N number of cubic *B*-spline functions. $p(r)$ shows directly the probability of finding a pair of electron densities at a particular distance '*r'*. Therefore, each spline function can be considered as a distance between a pair of stacked silicate layers.

The beauty of the GIFT method is that the form and structure factors can be determined simultaneously from the measured scattering data with the correction for the instrumental broadening effect [8, 9, 10]. Therefore, to evaluate the *p(r)* from the scattering curve, one has to consider the value of N, D_{max}, and λ_L. If there is a difference between $I_A(q)$ and $I_{exp}(q)$, then it is necessary to consider the effect of the structure factor.

D_{max} need not to be a perfect estimation of D. For rough estimation, $D_{max} \leq (\pi / q_1)$, where q_1 is the lowest scattering angle. A theoretical limitation for the number of functions $N = N_{max}$ follows from the sampling theorem. The main idea of the indirect Fourier transformation technique is to start with a large number of coefficients to guarantee a sufficient representation of the distance distribution function. For rough estimation, $N_{max} \leq (q_2.D_{max} / \pi)$, where, q_2 is the maximum scattering angle. The stabilization parameter restricts the oscillation of the spline functions, in other word, oscillation of *p(r)*. It should be chosen in such a way that the approximated scattering curve (determined on the basis of the *p(r)*) posses similar nature as the

experimental scattering curve. Then only one can conclude the *p(r)* related to the approximated scattering curve is the same as for the experimental scattering curve.

3. Determination of structure factor by applying modified Caillé theory conjugated with GIFT

The structure factor is determined according to the GIFT by using the modified Caillé theory for the lamellar phase. There are two theories that are applicable for the lamellar systems. The paracrystalline theory, a general theory for disorder of the first and second kind was developed by Hosemann & Bagchi [11] and Guinier [12]. This was the first attempt to deal with the disorder in multilamellar arrays. The paracrystalline theory of the first kind assumes that there are stochastic distance fluctuations around the well-defined mean layer positions of equal separation; i.e., the long range order is maintained. The paracrystalline theory of the second kind describes the fluctuations of bilayer separations relative to the nearest neighbors of ideally flat bilayers. These fluctuations are not correlated and the long-range periodic order collapses [12]. On the other hand, the Caillé theory developed on the basis of thermodynamic theory of DeGennes for the smectic liquid crystal is preferable because it takes into account the bending of the bilayers in addition to fluctuations in the mean spacings between bilayers [13]. The modified Caillé theory proposed by Zhang et al. takes into account the finite size of the lamellar stack [14, 15]. This modification does not affect the quantitative results obtained by the original Caillé theory, but the modification is necessary to obtain better quantitative fits to the data and particularly for extracting the correct form factor, which could be used later to obtain an electron density profile.

As long as the bilayer is unilamellar, there exists a direct relationship between the electron density profile in the perpendicular direction to the midplane of the bilayer and the form factor. The lateral arrangement of multilamellar bilayers is represented by the structure factor and can be determined by either the paracrystalline or Caillé theory with a few parameters. It is necessary to assume either a form factor or a structure factor for the evaluation of the scattering data according to the paracrystalline or modified Caillé theory.

Frühwirth et al. implemented the modified Caillé theory on the GIFT in order to analyze the stacked lamellar systems [16]. This model is defined by three parameters: the number of coherently scattering bilayers (n), the repeat distance (d) of bilayers, and the Caillé parameter (η_1). According to the modified Caillé theory, the structure factor can be expressed as

$$S(q) = n + \left\{ 2\sum_{m=1}^{n-1} (n-m)\cos(mqd)\exp\left[-\left(\frac{d}{2\pi}\right)^2 q^2 \eta\gamma \right] (\pi m)^{-(d/2\pi)^2 q^2 \eta_1} \right\} \qquad (24)$$

where γ is the Euler's constant (= 0.5772). Again, the Caillé parameter η_1 can be expressed as

$$\eta_1 = \frac{{q_1}^2 k_B T}{8\pi (K_c B)^{1/2}} \qquad (25)$$

where, $q=(2\pi/d)$ (26)

K_c is the bending modulus and B is the bulk modulus for compression. Since the two moduli can't be determined independently from the scattering data, one can consider η_1 as a measure of flexibility of the bilayers. According to the author, increasing the number of bilayers cause higher and narrower peaks, and increasing the Caillé parameter leads to a faster decay of the peaks of higher order.

4. Determination of electron density distribution profile

The electron density for the lamellae can be written as (provided one assumes the lamellae are homogeneous along the basal plane)

$$\rho(r) = \rho_0 . \rho_t(x) \tag{27}$$

Here, ρ_0 is a constant and x is the normal distance from the central plane in the lamellae. Therefore, $\rho_t(x)$ represents the electron density along the thickness cross-section profile. There are two different ways to determine the electron density profile. In the conventional method, one has to determine the scattering amplitude from the scattering intensity by a simple square root operation. However, the main problem is the determination of the right sign—the so-called phase problem. The second method is the estimation of the electron density from the distance distribution function by a convolution square root technique. This method doesn't suffer from the phase problem. Hosemann & Bagchi and Engel [11] showed that for the lamellar system, the convolution square root has a unique solution (except for a factor ±1) if the function has a finite range of definition and the function is symmetrical. Glatter used the convolution square root method in a different way. He deconvoluted the approximated electron density distribution in order to get the distance distribution function for the highly symmetric systems (sphere, cylinder, or lamella). According to him, the electron density is approximated in its range of definition by a linear combination of a finite number of functions that have to be linearly independent in this range and can be expressed as

$$\overline{\rho}(r) = \sum_{i=1}^{N} c_i \varphi_i(r) \tag{28}$$

where N is the number of functions, r is the normal distance from the center of symmetry, $\varphi_i(r)$ is the equidistant step function (cubic B-spline of zero order) with a width ΔR allowing the analytical integration of the overlap integrals, and c_i is the height of the step functions. Equation (28) corresponds to a nonlinear distance distribution function (presented in equation (3.29)), which can be solved by an interactive stabilized way to describe the $p(r)$ function obtained from indirect Fourier transformation / GIFT [6, 7, 17].

$$\overline{p}(r) = \sum_{i=1}^{N} V_{ii}(r) c_i^{\,2} + \sum_{i>k} V_{ik}(r) c_i c_k \tag{29}$$

Now if there is some deviation from the high symmetry, which is known as the polydispersity of the sample, then the *p(r)* determined by the deconvolution (DECON) method (done by DECON software) will be slightly different than the *p(r)* determined from GIFT. By estimating the amount of polydispersity one can achieve the best matching in *p(r)* determined by GIFT and DECON. Therefore, the electron density distribution derived from DECON should represent the experimental scattering curve.

5. Calculation of degree of anisotropy and mean orientation angle

In a densely packed system of particles, the positional ordering can develop a preferential orientation with respect to each other, especially when the particles are not spherical. The degree of orientation can be detected easily from the 2D SAXS patterns. An arc-profile is usually used to determine the orientation of crystals in a certain basal plane. The tdoa program uses the following equations to evaluate the degree of anisotropy and the mean orientation angle from azimuthal scattering profiles [18, 19].

A point on the azimuthal scan can be presented by a unit vector, u, such that $u_1 = \cos\beta$ and $u_2 = \sin\beta$, where β is the azimuthal angle. The anisotropy in the X-ray scattering pattern can be obtained by the weighted average of the second moment tensor of 'u' as

$$\langle uu \rangle = \begin{bmatrix} \langle u_1 u_1 \rangle \langle u_1 u_2 \rangle \\ \langle u_1 u_2 \rangle \langle u_2 u_2 \rangle \end{bmatrix} = \begin{bmatrix} \langle \cos^2\beta \rangle \langle \sin\beta\cos\beta \rangle \\ \langle \sin\beta\cos\beta \rangle \langle \sin^2\beta \rangle \end{bmatrix} \tag{30}$$

Here, <…..> represents an average weighted by the azimuthal intensity distribution and $\langle \cos^2\beta \rangle$ can be expressed as

$$\langle \cos^2\beta \rangle = \frac{\int_0^{2\pi} \cos^2\beta I(\beta) d\beta}{\int_0^{2\pi} I(\beta) d\beta} \tag{31}$$

The difference in eigenvalues ($\lambda_1 - \lambda_2$) of $\langle uu \rangle$ gives a measure of the anisotropy factor and can be expressed as

$$\lambda_1 - \lambda_2 = \sqrt{\left(\langle u_1 u_1 - u_2 u_2 \rangle\right)^2 + 4\langle u_1 u_2 \rangle^2} \tag{32}$$

The degree of anisotropy determined by the tdoa program is ($\lambda_1 - \lambda_2$) in percent.

The mean orientation angle or the average domain orientation angle can be expressed as

$$\overline{\chi} = \frac{1}{2}\tan^{-1}\left(\frac{2\langle u_1 u_2\rangle}{\langle u_1 u_1\rangle - \langle u_2 u_2\rangle}\right) \tag{33}$$

References

[1] Mittelbach R, Glatter O. Direct structure analysis of small-angle scattering data from polydisperse colloidal particles. J Appl Cryst 1998; 31: 600–08.

[2] Glatter O, Kratky O. Small Angle X-ray Scattering, Academic Press, London 1982.

[3] Schnablegger H, Singh Yashveer. A Practical Guide to Small Angle X-ray Scattering. Austria, Anton Par GmbH; 2006.

[4] Glatter O. A new method for the evaluation of small-angle scattering data. J Appl Cryst 1977; 10: 415–21.

[5] Glatter O. Data evaluation in small-angle X-ray scattering: Calculation of the radial electron density distribution by means of Indirect Fourier Transformation. Acta Phys Austriaca 1977; 47: 83–102.

[6] Glatter O. Convolution square root of band-limited symmetrical functions and its application to small-angle scattering data. J Appl Cryst 1981; 14: 101–08.

[7] Glatter O. Comparison of two different methods for direct structure analysis from small-angle scattering data. J Appl Cryst 1988; 21: 886–90.

[8] Bergmann A, Fritz G, Glatter O. Solving the generalized indirect Fourier transformation (GIFT) by Boltzmann simplex simulated annealing (BSSA). J Appl Cryst 2000; 33: 1212–16.

[9] Brunner-Popela J, Glatter O. Small-angle scattering of interacting particles. I. Basic principles of a global evaluation technique. J Appl Cryst 1997; 30: 431–42.

[10] Weyerich B, Brunner-Popela J, Glatter O. Small-angle scattering of interacting particles. II. Generalized indirect Fourier transformation under consideration of the effective structure factor for polydisperse systems. J Appl Cryst 1999; 32: 197–209.

[11] Hosemann R, Bagchi SN. Direct Analysis of Diffraction by Matter. Amsterdam, The Netherlands: North-Holland, 1962.

[12] Guinier A. X-ray Diffraction in Crystals, Imperfect Crystals and Amorphous Bodies. General Publishing Company, Ontario, Canada, 1994.

[13] Caille´ A, Seances CR. Acad. Sci. Ser. 1972, B274, 891. Also see the erratum in Gennes PG, The Physics of Liquid Crystals ~Oxford University Press, London, 1974, p. 336, Ref.20.

[14] Zhang R, Suter RM, Nagle JF. Theory of the structure factor of lipid bilayers. Phys Rev E 1994; 50: 5047–60.

[15] Zhang R, Tristram-Nagle S, Sun W, Headrick RL, Irving TC, Suter RM, Nagle JF. **Small-angle x-ray scattering from lipid bilayers is well described by modified Caillé theory but not by paracrystalline theory.** Biophysical J 1996; 70: 349–57.

[16] Frühwirth T, Fritz G, Freiberger N, Glatter O. Structure and order in lamellar phases determined by small-angle scattering. J Appl Cryst 2004; 37:703–10.

[17] Glatter O, Hainisch B. Improvements in real-space deconvolution of small-angle scattering data. J Appl Cryst 1984; 17:435–41.

[18] Caputo FE, Burghardt WR. Real-time 1−2 Plane SAXS measurements of molecular orientation in sheared liquid crystalline polymers. Macromolecules 2001; 34: 6684–94.

[19] Cinader JR, Burghardt WR. X-ray scattering studies of orientation in channel flows of a thermotropic liquid-crystalline polymer. J Polym Sci Part B: Polym Phys 1999; 37: 3411–28.